

Rochester Institute of Technology

RIT Digital Institutional Repository

Theses

5-31-2024

Tribological Performance of Ceramic on Textured Polyethylene Contact for Artificial Hip Implants

Sandhya Vaidyanathan
sv7416@rit.edu

Follow this and additional works at: <https://repository.rit.edu/theses>

Recommended Citation

Vaidyanathan, Sandhya, "Tribological Performance of Ceramic on Textured Polyethylene Contact for Artificial Hip Implants" (2024). Thesis. Rochester Institute of Technology. Accessed from

This Thesis is brought to you for free and open access by the RIT Libraries. For more information, please contact repository@rit.edu.

ROCHESTER INSTITUTE OF TECHNOLOGY

**Tribological Performance of Ceramic on Textured
Polyethylene Contact for Artificial Hip Implants**

Submitted by,

Sandhya Vaidyanathan

A Thesis Submitted in Partial Fulfillment of the Requirements for Master of Science
in Mechanical Engineering

Department of Mechanical Engineering

Kate Gleason College of Engineering

Rochester, New York

May 31, 2024

COMMITTEE APPROVAL:

Dr. Patricia Iglesias Victoria

Date: _____

Thesis Advisor

Department of Mechanical Engineering

Dr. Kathleen Lamkin-Kennard

Date: _____

Committee Member

Department of Mechanical Engineering

Dr. Rui Liu

Date: _____

Committee Member

Department of Mechanical Engineering

Dr. Sarilyn Ivancic

Date: _____

Department Representative

Department of Mechanical Engineering

ACKNOWLEDGMENTS

I am immensely grateful to Dr. Iglesias for giving me the opportunity to work in her lab and all the guidance and support she has offered throughout my time at RIT. Her in-depth knowledge in tribology, unwavering positivity, and confidence in me provided motivation through the entire process.

Special thanks to Prof. Salguero and Prof. Vazquez from the University of Cádiz, Dr. Nate Barlow from RIT's math department, and RIT's MECE Machine Shop for their help in supporting my research. I would also like to thank my fellow research students and lab buddies Alfonso Sierra Uran, Paarth Mehta, and Kiboi Davis for their help with equipment training, as well as all my friends who kept me sane throughout my engineering education.

Last but not least, I am grateful for my parents for their encouragement throughout my educational journey and for always believing in me.

Partial results from this work have been submitted for publication in the International Mechanical Engineering Congress & Exposition. All results from this work will also be compiled for submission to the journal, Tribology Letters.

ABSTRACT

Revision total hip arthroplasty (rTHA) is an expensive and surgically risky procedure that is necessary in the case of a failed primary total hip arthroplasty (pTHA). The cause of failure in artificial hip joints is often rooted in the tribological performance of the bearing surfaces such as increased wear and reduced lubrication. Surface texturing is a surface modification technique which has been studied for aerospace and automotive applications and has shown promise in the biomedical field of artificial human joints in the last two decades. Several studies have been done to assess the tribological performance of introducing surface micro-textures as a means of reducing friction and wear. However, not many studies are found in literature that focus on ceramic-on-polyethylene surfaces, specifically with the softer surface being textured. This thesis investigates the effects of surface texturing on the coefficient of friction and wear between a textured ultra-high molecular weight polyethylene (UHMWPE) plate and an alumina (Al_2O_3) ball. Surface textures with different combinations of dimple aspect ratio and texture densities are empirically studied in the boundary and/or mixed lubrication regime. Experiments are conducted via a reciprocating ball-on-flat friction tester. Microscopy and profilometry are done to understand the characterize the tribological behavior of the sliding surfaces. Additionally, a hydrodynamic lubrication model is implemented to examine the effects of the same surface textures on the maximum load-carrying capacity of the lubricant in the hydrodynamic lubrication regime.

TABLE OF CONTENTS

ACKNOWLEDGMENTS	2
ABSTRACT	3
TABLE OF CONTENTS	4
LIST OF FIGURES	6
LIST OF TABLES	7
NOMENCLATURE	8
1. PROBLEM INTRODUCTION	9
2. THE RESEARCH QUESTION	11
3. LITERATURE REVIEW	12
3.1. Biotribology.....	12
3.2. Artificial Hip Implants.....	13
3.3. Surface Texturing	15
4. OBJECTIVES OF THE PROPOSED WORK	19
5. EXPERIMENTAL WORK PERFORMED	20
5.1. Preparation of Textured Surfaces	20
5.2. Lubricant Properties	23
5.3. Tribological Tests	24
6. ANALYTICAL WORK PERFORMED	26
7. RESULTS AND DISCUSSION	29
7.1. Experimental Results	29
7.2. Analytical Results.....	33

8. CONCLUSION	36
9. SCOPE FOR FUTURE WORK	37
10. SOCIETAL CONTEXT	38
APPENDICES	39
Appendix A: Calculation of Lambda ratio, λ	39
Appendix B: Staggered-Grid Finite Difference Equations to solve the Hydrodynamic Lubrication Model.....	41
Appendix C: Two-way ANOVA Analysis for Coefficient of Friction Data	43
Appendix D: MATLAB Code	44
REFERENCES	49

LIST OF FIGURES

Fig. 3.1: Stribeck curve [9]	13
Fig. 5.1: 3D view of a textured bearing surface with texture features geometry labelled.....	20
Fig. 5.2: Microscopy of untextured sample (Sample Z)	21
Fig. 5.3: (a) 3D profilometer image of a section of textured sample D, (b) profile of dimple cross-section	22
Fig. 5.4: Viscosity vs. shear rate measurements for artificial synovial fluid across three trials	23
Fig. 5.5: a) Custom-built tribometer, (b) close-up of pin and specimen, and (c) schematic of apparatus.....	24
Fig. 6.1: Schematic of the lubrication model showing (a) cross-sectional view and, (b) top view.....	26
Fig. 6.2: Examples of non-dimensional local bearing spacing for (a) Sample A, (b) Sample E, and (c) Sample K.....	28
Fig. 7.1: Summary of results for friction data of the different textured samples	29
Fig. 7.2: Coefficient of friction values over distance of (a) sample A, and (b) sample L	30
Fig. 7.3: Wear scars for textured samples	31
Fig. 7.4: Longitudinal cross-section of wear tracks for (a) the untextured sample, (b) sample A, and (c) sample L from profilometry	32
Fig. 7.5: Hydrodynamic pressure over a column of three dimples.....	33
Fig. 7.6: Non-dimensional load-carrying capacity as a function of dimple aspect ratio and texture density	34

LIST OF TABLES

Table 5.1: Samples used in this study, identified by their aspect ratio ε and texture density S_p , along with their optical microscopy images	21
Table 5.2: Tribometer testing parameters.....	25
Table 7.1: Coefficient of friction values with percent differences of the different textured samples compared to the untextured sample	30

NOMENCLATURE

ε	=	Dimple aspect ratio
S_p	=	Texture density
r_p	=	Dimple radius
r_l	=	Unit cell length
h_p	=	Dimple depth
U	=	Relative sliding velocity
c	=	Minimum clearance
h	=	Local clearance
N	=	Number of dimples per column
p_0	=	Ambient pressure
p	=	Lubricant pressure
η	=	Dynamic viscosity

1. PROBLEM INTRODUCTION

Total hip arthroplasty (THA) is a surgical procedure used to treat chronic hip pain and disability, which could be caused by arthritis or traumatic injury. The procedure involves replacing the damaged femoral head and cartilage with prosthetic components that generally consist of a stem that is attached to the femoral bone, a ball that is placed on the upper part of the stem, a socket that is attached to the acetabular portion of the pelvis, and a spacer or liner that is inserted between the prosthetic ball and socket [1,2]. In the case of a failed primary total hip arthroplasty (pTHA), the only therapeutic action is a revision total hip arthroplasty (rTHA) to replace the failed components from the original surgery. The rTHA does not only create a financial burden for the patients and the national healthcare system, but also poses surgical risks including a higher rate of sepsis, prosthetic joint infection, more blood loss and transfusion, and medical complications compared to the pTHA [3]. One of the leading causes for the limited life-span of the pTHA components, often spanning 10 to 20 years after surgery, is aseptic loosening which is the failure of fixation of a prosthetic component in the absence of an infection. Wear debris from the implant causes particle-induced osteolysis around it which can result in aseptic loosening of the components [4]. Thus, it is crucial to investigate the properties and design of artificial implant materials to improve tribological performance.

Surface modifications techniques such as surface texturing, surface coating, and surface grafting have been widely studied for different applications to achieve optimal tribological performance without changing bulk material and have recently found their way in the field of artificial hip implant design. Surface texturing refers to the process of creating artificial asperities with defined geometry and distribution on the bearing surface. Based on different conditions such as load, relative velocity, dimple aspect ratio, and texture density, surface texturing has shown improved tribological performance by acting as a lubricant reservoir, increasing hydrodynamic pressure between sliding surfaces, storing wear debris, and/or decreasing sliding surface contact area [5]. Different material combinations such as metal-on-metal (MoM), metal-on-polyethylene (MoP), ceramic-on-polyethylene (CoP), ceramic-on-ceramic (CoC), and metal-on-ceramic (MoC) display different wear mechanisms and therefore, respond differently to surface textures. The availability of such a wide variety of artificial hip implant designs and biomaterials in the market requires research to explore the effects of surface texturing for each of these different cases.

Previous studies with hard-on-soft coupling have generally experimented with the hard surface being textured. In a 2019 study, Nečas et al. [6] reversed this by experimenting with a dimpled ultra-high molecular weight polyethylene (UHMWPE) acetabular cup articulating with four smooth femoral heads of metal and different ceramics. Their work showed reduction in friction in the textured samples across all the materials during the running-in phase. Moreover, not much literature exists on surface-textured CoP surfaces, specifically. Further investigation of the use of a dimpled UHMWPE surface articulating with a hard surface like ceramic can provide new insights on the friction and wear mechanisms. The proposed thesis work seeks to explore the tribological performance of a dimpled soft polyethylene surface articulating with a hard ceramic ball to characterize and explain friction and wear behavior.

2. THE RESEARCH QUESTION

Several studies have shown the positive tribological impact of adding textures to sliding surfaces. The main contribution of this work will be to show how adding micro-textures to the softer surface in a CoP contact will affect the coefficient of friction and wear volume. This thesis work will seek answers to the following research questions:

- i. Does a textured UHMWPE surface articulating against a ceramic ball exhibit lower coefficient of friction and wear than an untextured UHMWPE surface? If so, what mechanisms improve tribological performance?
- ii. What combination of dimple aspect ratio and texture density performs best tribologically?

3. LITERATURE REVIEW

3.1. Biotribology

Biotribology refers to the science of interacting surfaces in relative motion in the context of the human or an animal body and encompasses concepts such as friction, wear, and lubrication. The failure of artificial hip implants is often due to wear-related problems such as aseptic loosening [4]. Thus, it is important to get a good grasp of the key concepts in biotribology to improve current artificial implant designs and propose new solutions.

Friction is commonly defined as the resistance to relative motion between two surfaces in contact. As polished as a surface may seem, at the microscopic level, all surfaces contain asperities which induce friction, mainly due to local adhesion and deformations that take place at asperity junctions when two surfaces are in contact and move relative to one another [7]. Sliding or kinetic friction force is proportional to the normal force at the interface and can be expressed as shown in Eq. (3.1), where F_f is the frictional force, N is the normal force, and μ is the coefficient of friction.

$$F_f = \mu N \quad (3.1)$$

Wear refers to the gradual removal of material at the surface of a solid. Several wear mechanisms have been identified and defined in tribology studies, but adhesive and abrasive wear are most common types in the context of hip implants [7]. Adhesive wear occurs due to local welding between asperities that are broken away from one another due to sliding motion. Abrasive wear occurs when a hard surface moves along a soft surface. This can cause a two-body abrasion where the hard surface abrades the soft one, or a three-body abrasion where a hard particle trapped between the two surfaces abrades either or both surfaces.

Lubrication is introduced to assist in sliding movement and to reduce energy losses due to friction. In animal joints, synovial fluid acts as a natural lubricant enabling smooth movement. Lubricants get into the spaces between the surface asperities and reduce asperity-to-asperity interactions or completely separate them. In the boundary lubrication regime, which occurs under high load and low speed conditions, the lubricant pressure is not sufficient to separate the two surfaces or to support the load. Thus, there is a considerable amount of asperity contact between the two

surfaces. In the hydrodynamic or full-film lubrication regime, which occurs under low load and high-speed conditions, the sliding surfaces are completely separated due to the lubricant pressure. This occurs when the lubricant forms a converging wedge as the two surfaces slide relative to each other, thus forming a lifting pressure [8]. The mixed-film lubrication regime is a combination of both the hydrodynamic and the boundary lubrication regimes. The Stribeck curve, shown in Fig. 3.1, is a fundamental concept in tribology which graphically represents the variation in the coefficient of friction over the entire spectrum of the different lubrication regimes. The Hersey number, which is plotted in the x -axis, represents a dimensionless lubrication parameter, and includes the lubricant's dynamic viscosity, η , the entrainment speed of the lubricant, N , and the normal load per length of contact, P .

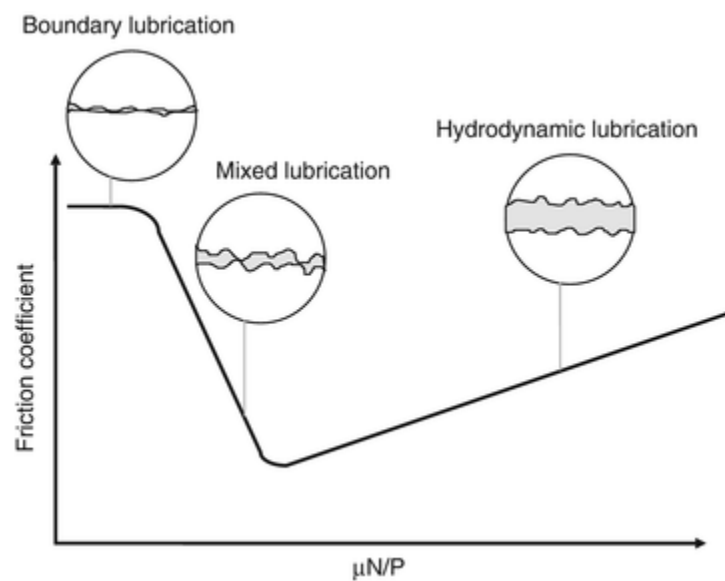


Fig. 3.1: Stribeck curve [9]

3.2. Artificial Hip Implants

Artificial hip implants consist of a femoral head articulating with an acetabular cup. The head can be made of ceramic or metal and the acetabular liner/cup can be made of ceramic, metal, or polymer. Metals were one of the first materials used in the early stages of development of artificial hip implants and metal alloys such as titanium alloys and cobalt-chromium-molybdenum (CoCrMo) alloys have commonly been used in this application due to their biocompatible nature and excellent

mechanical and corrosive properties [10]. Polymers, particularly UHMWPE, are known for their high wear resistance and low friction properties. However, acetabular liners/cups made of polyethylene also generate debris when implanted that is attacked by the body's immune system causing osteolysis and consequently, mechanical loosening of the implant [11]. Ceramics, such as alumina (Al_2O_3) and zirconia-toughened alumina, were introduced to THA to overcome this issue of polyethylene wear and due to the inert nature of their wear particles along with their hardness and scratch resistance [12].

The MoM coupling gained popularity in the 1960s and 1970s due to its low wear rates compared to the MoP coupling. Despite its positive tribological performance, MoM has become extremely uncommon in the past decade due to the potential for an increased release of metal ions into the bloodstream, which can be toxic when highly concentrated [11,13]. With Sir John Charnley's pioneering efforts, the MoP coupling emerged as a more common choice with the Co-Cr femoral head articulating with an UHMWPE acetabular cup being one of the most acceptable bearing surface couples today due to its relatively good long-term performance [14]. However, concerns of polyethylene wear causing osteolysis due to wear debris have prompted ongoing research to improve the durability of this material pair. The CoC coupling has shown promise due to the biologically inert nature of ceramic wear particles but comes with its own share of complications such as squeaking and brittle fracture [15]. Lastly, the CoP coupling combines the inert ceramic component with the soft polyethylene component while mitigating the risks associated with metal debris. Due to the lower Young's modulus of polyethylene compared to the harder metals and ceramics, and thus its ability to undergo deformations more easily, this coupling may benefit from an enhanced fluid layer and potentially exhibit lower friction from smoothening caused during natural movement [16]. Heckmann et al. studied the trends of hip implant bearing surface selection in the United States and found that CoP saw a steady year-by-year increase from being 11.1% of the total cases in 2007 to 50.8% by 2014, surpassing even MoP which accounted for 42.1% of the total cases that year. MoM peaked in 2008 at 40.1% of the total cases and only accounted for 4.0% of the cases by 2014 with CoC closely following it at 3.1% of the total cases [17].

3.3. Surface Texturing

Surface texturing is a surface modification technique which has slowly gained traction in the field of orthopedic biomaterials in the past two decades. Although not directly related to tribology, several studies have shown their success in enhancing the biocompatibility and osseointegration of the implant by improving osteoblast adhesion, leading to better integration with the surrounding bone tissue and improving the implant's stability [18,19]. Surface textures have been used successfully in a variety of engineering applications such as cutting tools, piston and ring cylinders, and journal bearings as a means of reducing friction and wear [20]. With aseptic loosening being the leading cause of failures in THA and being rooted in the production of wear particles, surface textures have been investigated as a means of reducing friction and wear. The integration of advanced surface texturing methods could lead to the development of more durable and biocompatible artificial hip joints, ultimately improving patient outcomes.

Various processes exist to develop surface textures for different types of orthopedic materials including molding, laser-based techniques, conventional machining, and electrochemical processes. Laser surface texturing (LST) is a common method widely used by researchers for its efficiency, controllability, ease of automation and high processing speed [21,22]. The process involves ablating the work surface with a high-energy beam of laser causing the material to melt and vaporize, thus modifying the surface topography. Some drawbacks of the method include the build-up of ablated material around the dimple edges and local modification of the material's properties especially in polymers [23]. CNC micro-milling is a viable alternative that makes use of small indenters which can come in different shapes combined with different indentation loads and material hardness to produce textures of different depths [24]. Alternatively, electrochemical processes selectively etch away unmasked material to create texture features.

To evaluate the effectiveness of these textured surfaces, wear tests with varying levels of sophistication are utilized in tribological research. Wear joint devices test real prostheses in an environment that simulates physiological conditions whereas wear screening devices provide a way of quickly testing the materials studied while approximately replicating the same wear mechanisms that occur with a given pair of materials [25]. Hip joint simulators are wear joint devices that usually utilize a spherical femoral head articulating with a hemispherical acetabular shell and replicate the complex

motions and loads that create tribological conditions similar to those experienced by hip joints in the human body [26]. These simulators are invaluable in offering a realistic assessment of wear behavior, especially over extended periods. Dong et al. performed hip simulator tests using an inverted pendulum hip joint simulator which used angular velocity sensors to collect oscillation data and calculated the coefficient of friction using the linear decay of the pendulum [27]. They reported a 20% reduction in the coefficient of friction between the head and cup for the MoP micro-textured surface. Alternatively, pin-on-disk tribometers are widely used wear screening devices in tribological research due to their simplicity and cost-effectiveness. The method involves using a pin that represents the femoral head and a rotating disk that represents the acetabular cup, sliding against each other under controlled conditions of load, frequency, distance, and environment. Young et al. performed one of the earlier studies using a pin-on-disk tribometer to evaluate the performance of CoCrMo pins sliding against textured UHMWPE disks and measured the coefficient of friction and wear [28]. The tribometer made use of strain gauges arranged in the Wheatstone bridge configuration to indirectly measure the frictional force between the two surfaces. They reported a reduction in the coefficient of friction of the textured surface, but an increase in wear debris. Other wear screening devices include ball-on-flat, ring-on flat, and cylinder-on-flat tribometers.

Based on the bearing operating conditions such as load and sliding relative velocity, as well as texture geometry such as shape, aspect ratio, and texture density, the literature documents three main functions that surface textures perform in order to improve tribological performance [24]. Generally, deep texture features act as lubricant reservoirs and reduce friction and wear by reserving and supplying lubricant under starvation conditions during boundary or mixed lubrication conditions. Studies by Lee et al. [29] and Tarabolsi et al. [30] reported that the dimples stored wear debris produced during articulation, thus reducing three-body abrasive wear. Similarly, Sufyan et al. [31] and Pratap and Patra [32] attributed improved tribological performance to the dimples functioning as lubricant reservoirs and suggested a shift from the boundary lubrication to the mixed lubrication regime to be the primary mechanism for friction reduction. Shallow texture features generally boost hydrodynamic lubrication by increasing the lubricant film pressure, consequently increasing lubricant film thickness. This, in turn, reduces contact between the bearing surfaces, thus reducing friction and wear. This effect is seen in studies done by Borjali et al. [1], Dougherty et al. [33], Kashyap and Ramkumar [34], Cho and Choi [35], and Roy et al. [36]. Lastly, texture features can also reduce the nominal contact

area between the bearing surfaces if contact occurs under boundary lubrication conditions as shown by Cuervo et al. [37], Kustandi et al. [38], and Wei et al. [39]. These are driven by the texture density rather than the dimple aspect ratio.

Looking specifically at hard-on-soft material combinations, Ito et al. carried out experiments on a dimpled metal Co-Cr alloy femoral head against an UHMWPE socket using a hip joint simulator [40]. They demonstrated a reduction in the coefficient of friction by 17% and a reduction in wear by 69% while using the dimpled surface and attributed this improved performance to the dimple storing wear debris, thus reducing abrasive wear. Moreover, lubricant stored in these dimples was thought to be dispensed as a result of its viscosity, thereby providing a continuous supply of lubrication. Similarly, a more recent study was done by Borjali et al. using a pin-on-disk test [1]. They tested a dimpled CoCrMo disk articulating with an UHMWPE pin using micro-textures of different aspect ratios and texture densities. They reported a reduction in polyethylene wear across all the micro-textured disks compared to the smooth disks and showed through surface topography measurements that the UHMWPE pin articulated against the textured CoCrMo disk was almost completely intact as compared to the smooth CoCrMo disk. This was said to be the result of micro-hydrodynamic bearing created by the micro-textures which increases the lubricant film thickness, thus reducing friction and polyethylene wear.

Although not as commonly studied as the MoP coupling, a few studies have been conducted on the CoP coupling. Choudhury et al. experimented with an UHMWPE pin rolling on a dimpled alumina plate [41]. They documented an increase in both the coefficient of friction and polyethylene wear explaining that this may have been due to ceramic's much greater Young's modulus compared to UHMWPE. The hard ceramic does not deform as much as the softer UHMWPE, as a result of which the deformed UHMWPE comes in contact with the texture edges on the ceramic surface, causing abrasive wear and an increase in the coefficient of friction. Nečas et al. reversed this and evaluated the tribological performance of a smooth ceramic head articulating against a dimpled UHMWPE acetabular liner [6]. They reported a reduction in the coefficient of friction with the textured surface across all the different materials they tested, including the alumina head against the texture UHMWPE liner. In addition to the dimples acting as lubricant reservoirs, they suggested that this reduction in friction was due to the diminishing of the dimples on the UHMWPE surface, eventually leading to a reduction of the contact asperity ratio, enabling the implant to operate smoothly

for longer. Nevertheless, polyethylene wear is still a concern and needs to be further investigated especially in terms of the micro-textures boosting hydrodynamic lubrication and how this is affected by the deformation of polyethylene. This research study seeks to explore the tribological performance of a dimpled soft UHMWPE surface sliding against a hard alumina ball to explain friction and wear behavior.

4. OBJECTIVES OF THE PROPOSED WORK

The overarching goal of the proposed work is to examine the tribological effects of adding textures to the softer surface in an artificial hip implant and to propose possible mechanisms that might be in play. To this end, the objectives of this study are as follows:

- i. To examine the tribological performance of a textured UHMWPE surface against a ceramic ball through tribometer testing
- ii. To analyze coefficient of friction and wear results and provide explanations of the mechanisms that the UHMWPE surface undergoes that describe its tribological performance
- iii. To implement the hydrodynamic lubrication model that describes the load-carrying capacity of the lubricant for different dimple geometries

5. EXPERIMENTAL WORK PERFORMED

5.1. Preparation of Textured Surfaces

In order to simulate artificial hip joint surfaces, an UHMWPE plate (Transglass Productos Plásticos, Spain) with a density of 0.93 g/cm^3 , 63 Shore-D, and an initial average roughness of $R_a \sim 0.064 \text{ }\mu\text{m}$ trimmed into smaller blocks were used to represent the acetabular portion. The femoral head was represented by a 6mm diameter 92% alumina ball (MSE Supplies LLC, USA).

Surface textures were created by Prof. Jorge Salguero and Prof. Juan Manuel Vazquez from the University of Cádiz, Spain on the surface of the UHMWPE plates using a LS-MARKPRO SC-IR 21002 femto-second infrared laser. Each circular dimple was obtained by the irradiation of nine concentric circles with an increasing of $5 \text{ }\mu\text{m}$ radius. Considering the nominal spot diameter of $25 \text{ }\mu\text{m}$, a modified $100 \text{ }\mu\text{m}$ circular area in diameter was achieved. Different texture densities were developed using a matrix pattern of the circular dimples with center-to-center distances of 100, 150, 250, and $300 \text{ }\mu\text{m}$ as shown in Table 5.1. For samples A-D, a nominal depth of $30 \text{ }\mu\text{m}$ was targeted with laser irradiation parameters of 30W power, 250 kHz pulse rate, and a 200 mm/s scan speed. For samples E-H, a nominal depth of $12 \text{ }\mu\text{m}$ was targeted with laser irradiation parameters of 40W power and 50 kHz pulse rate. For samples I-L, a nominal depth of $6 \text{ }\mu\text{m}$ was targeted with laser irradiation parameters of 30W power and 50 kHz pulse rate. The textures are described by the aspect ratio ε , which is the ratio of dimple depth to dimple diameter and the texture density S_p , which represents how closely packed the dimples are relative to each other as described in Fig. 5.1.

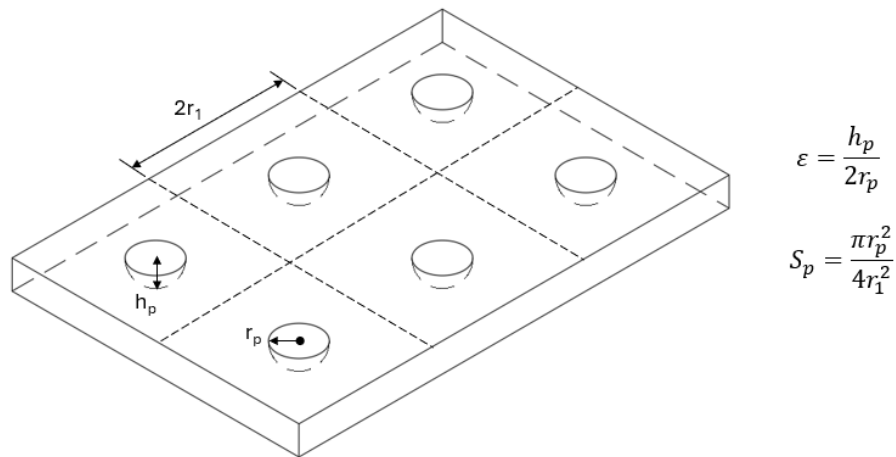


Fig. 5.1: 3D view of a textured bearing surface with texture features geometry labelled

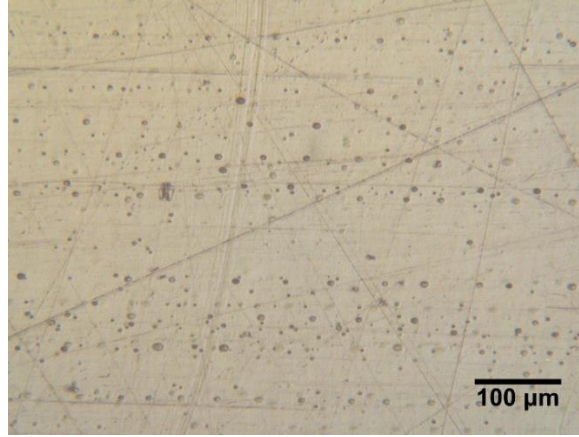
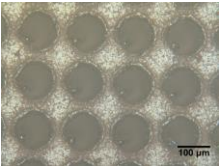
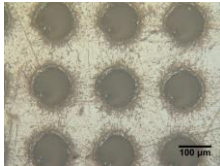
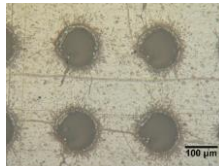
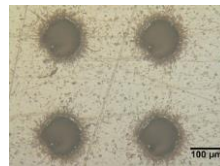
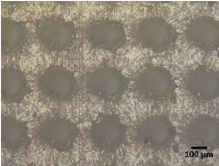
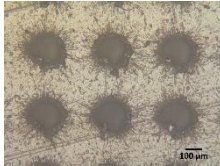
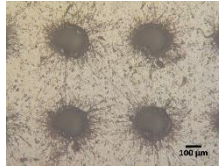
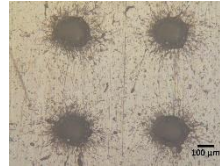
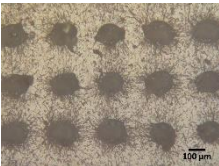
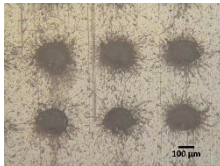
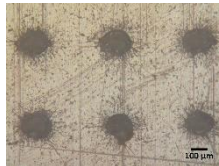
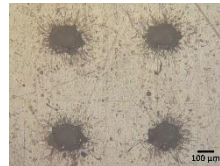


Fig. 5.2: Microscopy of untextured sample (Sample Z)

Table 5.1: Samples used in this study, identified by their aspect ratio ε and texture density S_p , along with their optical microscopy images

<p>Sample A $\varepsilon = 0.30$ $S_p = 0.35$</p> 	<p>Sample B $\varepsilon = 0.30$ $S_p = 0.20$</p> 	<p>Sample C $\varepsilon = 0.30$ $S_p = 0.13$</p> 	<p>Sample D $\varepsilon = 0.30$ $S_p = 0.09$</p> 
<p>Sample E $\varepsilon = 0.12$ $S_p = 0.35$</p> 	<p>Sample F $\varepsilon = 0.12$ $S_p = 0.20$</p> 	<p>Sample G $\varepsilon = 0.12$ $S_p = 0.13$</p> 	<p>Sample H $\varepsilon = 0.12$ $S_p = 0.09$</p> 
<p>Sample I $\varepsilon = 0.06$ $S_p = 0.35$</p> 	<p>Sample J $\varepsilon = 0.06$ $S_p = 0.20$</p> 	<p>Sample K $\varepsilon = 0.06$ $S_p = 0.13$</p> 	<p>Sample L $\varepsilon = 0.06$ $S_p = 0.09$</p> 

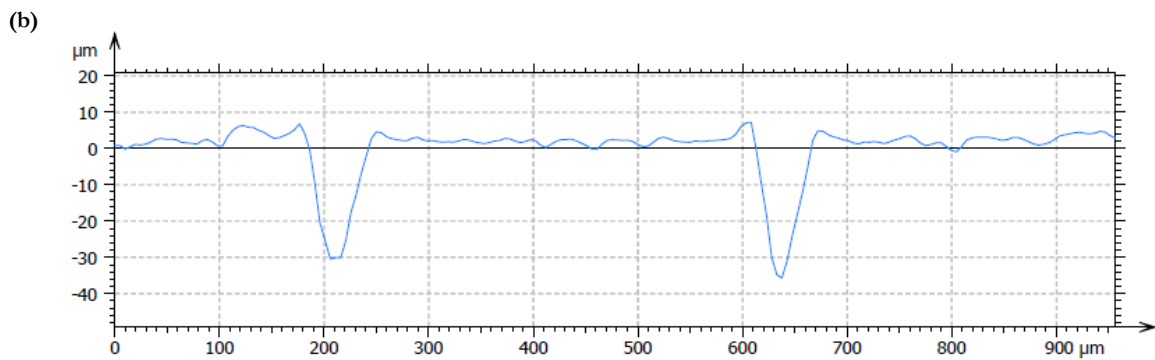
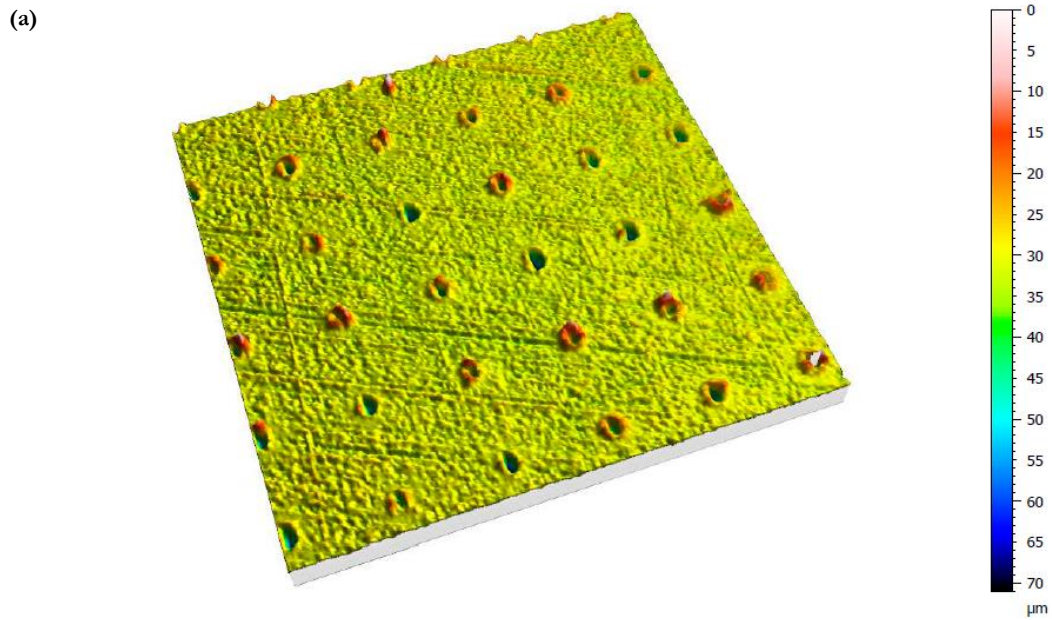


Fig. 5.3: (a) 3D profilometer image of a section of textured sample D, (b) profile of dimple cross-section

After the texturing process, the focus variation microscopy (FVM) technique on an Alicona IF G5+ was used to characterize the depth and geometry of the irradiated dimples as shown in Fig. 5.3. It is to be noted that as can be seen in both the profile and the cross-section view, the laser texturing process resulted in the formation of protuberances around the dimples on the UHMWPE sample due to the accumulation of deformed material, which could lead to an increased coefficient of friction and wear rate in the running-in phase.

5.2. Lubricant Properties

Commercially-available artificial synovial fluid (Biochemazone) was used as the lubricating fluid. After some initial testing on a Brookfield Viscometer, it was determined that the fluid was a non-Newtonian fluid, similar to human synovial fluid. Thus, the viscosity of the fluid was measured using TA Instruments' Discovery Hybrid Rheometer with a cone and plate geometry. Viscosity measurements were taken at room temperature ($\sim 24^{\circ}\text{C}$) for shear rates from $1 [\text{s}^{-1}]$ to $100 [\text{s}^{-1}]$. An exponential curve fit was used to extrapolate the viscosity measurement at the $2 [\text{s}^{-1}]$ shear rate which corresponds to the $2 [\text{Hz}]$ frequency at which the tribometer was run. An average viscosity measurement of $0.0497 [\text{Pa}\cdot\text{s}]$ was calculated across three trials at the $2 [\text{s}^{-1}]$ shear rate.

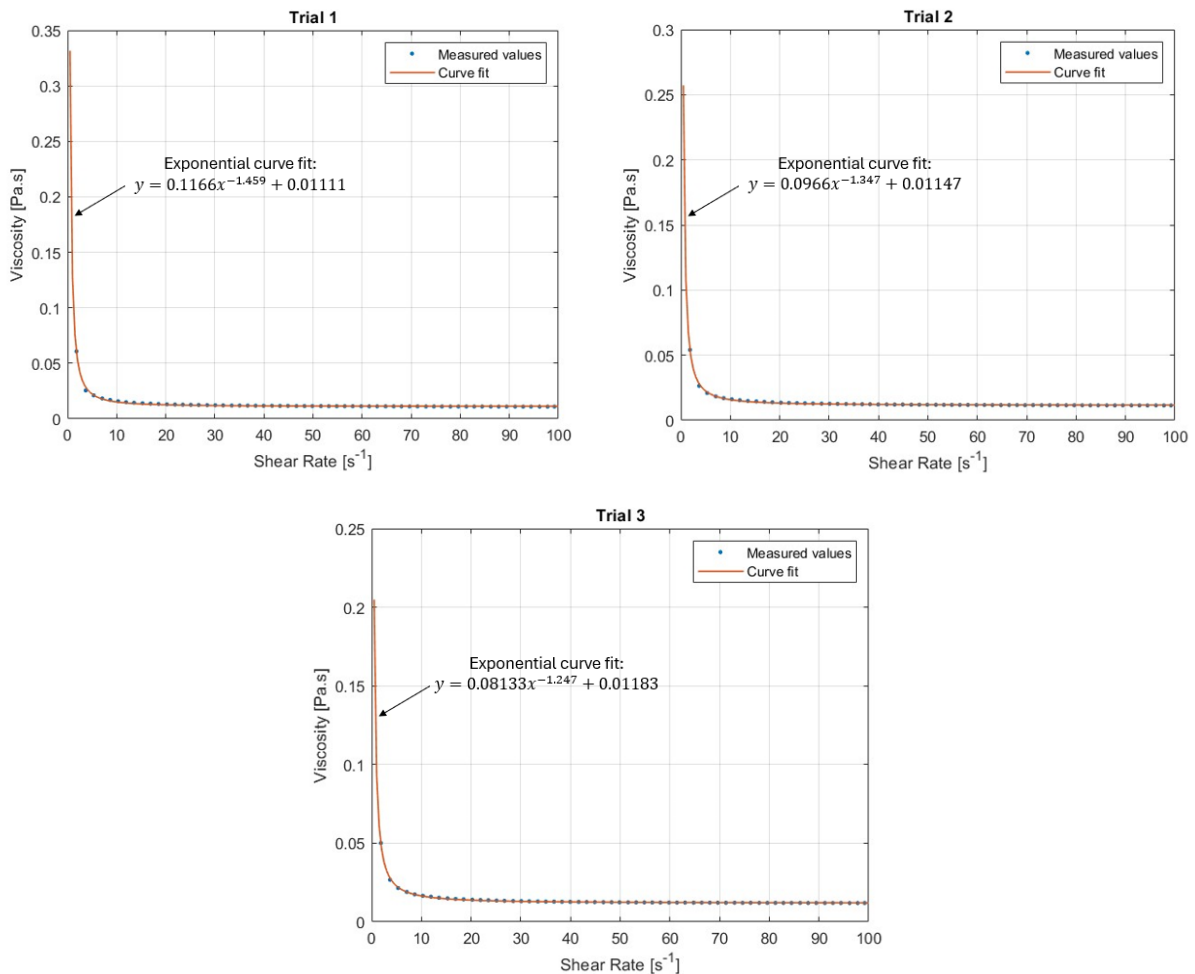


Fig. 5.4: Viscosity vs. shear rate measurements for artificial synovial fluid across three trials

5.3. Tribological Tests

Friction testing was carried out on a custom-built ball-on-flat reciprocating tribometer designed as per ASTM G133. The apparatus, shown in Fig. 2, consists of a pin that holds the Al_2O_3 ball and a sample holder which holds the PE1000 block. A linear voice coil actuates the specimen holder back and forth at a set frequency and stroke length. Strain gauges attached to the tribometer arm are used to measure the friction forces generated during sliding and converted into coefficient of friction in LabVIEW. Before running tests, several stabilizing tests were performed as per the tribometer manual to determine the amount of noise in the system. The determined value was then subtracted from the coefficient of friction during subsequent tests.

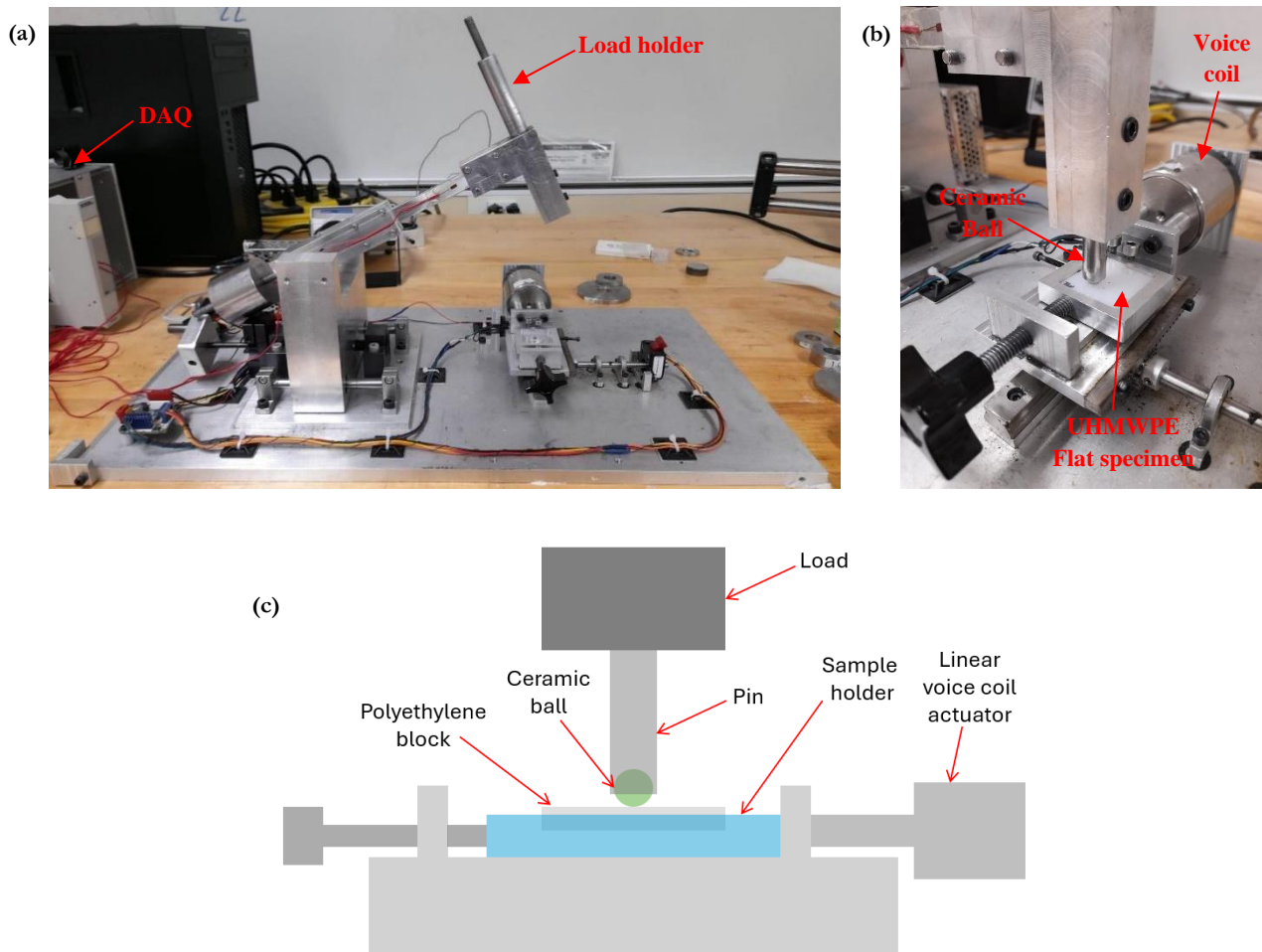


Fig. 5.5: a) Custom-built tribometer, (b) close-up of pin and specimen, and (c) schematic of apparatus

Three tests were carried out for each texture to minimize experimental error. The tests were conducted at a frequency of 2 Hz and a stroke length of 5 mm for one hour, which translates to a sliding speed of 0.02 m/s and a total sliding distance of 72 m. The normal load was kept constant at 3 N, which corresponds to a maximum Hertz contact pressure of 27 MPa. For the untextured surfaces, these parameters correspond to the boundary lubrication regime with lambda ratio, $\lambda < 1$ as calculated in Appendix A. ~0.2 mL of artificial synovial fluid was placed between the contact surfaces for lubrication in the beginning of the test. These parameters were informed by prior studies and the limitations of the apparatus. Although the peak contact pressures in the normal human hip joint anatomy are only within the ranges of 2 MPa to 9 MPa [42], the loads used to reach such low pressure values produced wear tracks that were too superficial for comparison. The sliding velocity was selected to be similar to previous experiments run by other researchers [24].

Table 5.2: Tribometer testing parameters

Load	[N]	5
Stroke length	[mm]	5
Frequency	[Hz]	2
Equivalent sliding speed	[m/s]	.02
Max. Hertz contact pressure	[MPa]	27

Wear tracks resulting from the tribometer testing were imaged using an Olympus BH-2 Optical Microscope. Images were taken at three spots along the wear scar. Images of the alumina ball were also taken after tribometer testing using an Olympus SZX-12 Optical Microscope. In order to study the 3D morphology of the wear track, a Nanovea ST-400 profilometer with a resolution rate of 1000 Hz was used.

6. ANALYTICAL WORK PERFORMED

Intentionally created micro-textures on one of the sliding surfaces has shown to increase the lubricant's load-carrying capacity based on the dimple shape, aspect ratio, texture density, and operating conditions, thus, reducing friction. Fig. 6.1 shows the set-up of the model that is implemented and is based on work done by Qiu et al. [43] and Chyr et al. [44]. To simplify the analysis, the ball-on-plate contact is approximated as a parallel slider bearing. The textured UHMWPE surface is represented by a column of N dimples. The top surface is untextured and moves relative to the bottom textured surface at a velocity U . It is assumed that the minimum spacing c between the surfaces is enough to avoid asperity contact and hydrodynamic lubrication is maintained throughout. Each dimple has an identical spherical shape and is positioned in the center of a square cell of width, $2r_1$. The dimple diameter r_p is automatically adjusted using user input values of S_p . No slip is assumed at the solid boundaries.

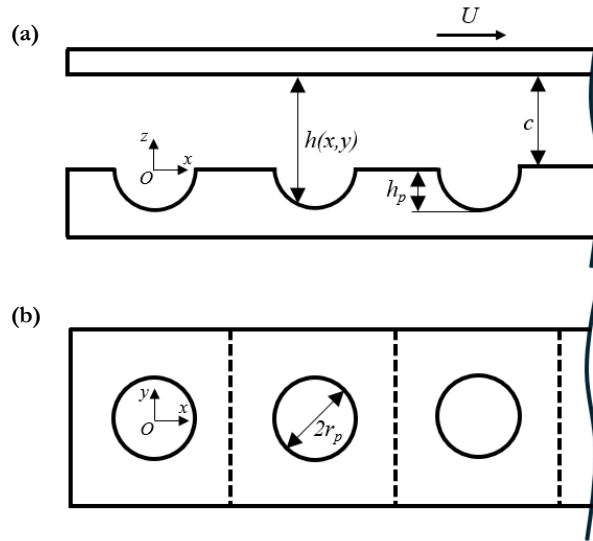


Fig. 6.1: Schematic of the lubrication model showing (a) cross-sectional view and, (b) top view

The relationship between the bearing spacing and the lubricant pressure can be expressed in the form of the steady-state two-dimensional incompressible Reynolds' equation,

$$\frac{\partial}{\partial x} \left(h^3 \frac{\partial p}{\partial x} \right) + \frac{\partial}{\partial y} \left(h^3 \frac{\partial p}{\partial y} \right) = 6\eta U \frac{dh}{dx} \quad (6.1)$$

where x and y are indicated in Fig. 6.1(b), $p(x, y)$ is the local bearing space, $h(x, y)$ is the local bearing spacing, η is dynamic viscosity of the artificial synovial fluid, and U is the relative sliding velocity between the two surfaces. Eq. (5.1) is non-dimensionalized and re-written as:

$$\frac{\partial}{\partial X} \left(H^3 \frac{\partial P}{\partial X} \right) + \frac{\partial}{\partial Y} \left(H^3 \frac{\partial P}{\partial Y} \right) = \frac{\lambda}{\delta^2} \frac{dH}{dX} \quad (6.2)$$

where $X = \frac{x}{r_p}$, $Y = \frac{y}{r_p}$, $P(X, Y) = \frac{p(x, y)}{p_0}$, $H(X, Y) = \frac{h(x, y)}{c}$, $\delta = \frac{c}{2r_p}$, and $\lambda = \frac{3\eta U}{2r_p p_0}$.

The inlet and outlet of the column of N dimples are maintained at ambient pressure, p_0 . The following boundary condition are imposed on the square cell:

$$P \left(-\frac{r_1}{r_p}, Y \right) = P \left(\left(N - \frac{1}{2} \right) \frac{2r_1}{r_p}, Y \right) = 0 \quad (6.3)$$

$$\frac{\partial P}{\partial Y} \left(X, -\frac{r_1}{r_p} \right) = \frac{\partial P}{\partial Y} \left(X, \frac{r_1}{r_p} \right) = 0 \quad (6.4)$$

The cavitation condition is set to the following:

$$p = p_{cav} = 0, \text{ if } p < 0$$

The non-dimensional local spacing, $H(X, Y)$ between the two surfaces for spherical dimples is given by [43]:

$$H(X, Y) = \begin{cases} 1 & \text{if } X^2 + Y^2 > 1 \\ 1 + \frac{1}{2\delta} \sqrt{\left(\varepsilon + \frac{1}{4\varepsilon} \right)^2 - (X^2 + Y^2)} - \frac{1}{2\delta} \left(\frac{1}{4\varepsilon} - \varepsilon \right) & \text{if } X^2 + Y^2 \leq 1 \end{cases} \quad (6.5)$$

Fig. 6.2 shows examples of the plots for a single dimple geometry's non-dimensional local spacing, $H(X, Y)$ for three different textures.

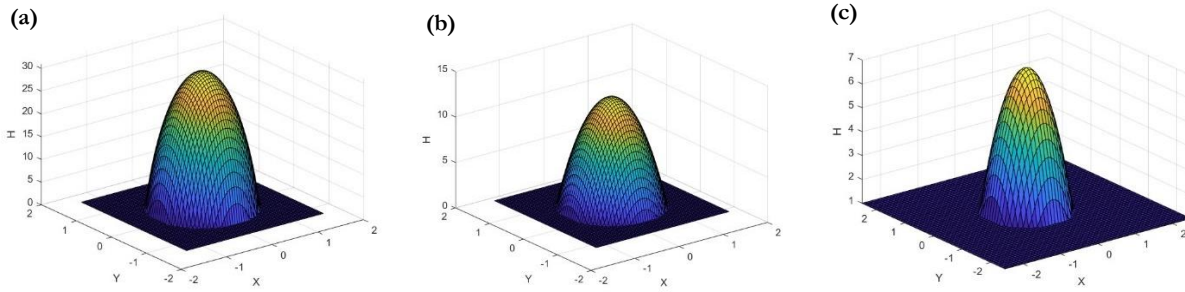


Fig. 6.2: Examples of non-dimensional local bearing spacing for (a) Sample A, (b) Sample E, and (c) Sample K

Appendix D contains the MATLAB code that has been developed that allows the user to input different values of dimple aspect ratio, texture density, and number of dimples per column and outputs the non-dimensional local spacing. Eqn. (6.2) is solved for a column of seven dimples using a central discretization staggered-grid finite difference method and the Gauss-Seidel iterative method with a successive over-relaxation factor of 1.4 [45]. The pressure calculation is iterated until the relative change between two successive iterations of the pressure calculation in each grid is less than 10^{-2} . The non-dimensional load carrying capacity is calculated and plotted by taking the average value of the pressure matrix.

7. RESULTS AND DISCUSSION

7.1. Experimental Results

In this study, the effect of different texture densities and dimple aspect ratios was evaluated for ceramic on textured polyethylene contacts and compared against an untextured contact. As illustrated in Fig. 7.1, the majority of the textured samples outperform the untextured sample with the exception of samples A, B, C, and E in terms of the average coefficient of friction value. A significant 24% reduction in the average coefficient of friction value is observed in sample L, which has the lowest aspect ratio and texture density out of all the samples, compared to the untextured sample. On the other hand, there is a 70% increase in the average coefficient of friction value in sample A.

A clear trend is observed in the relationship between dimple spacing and the average coefficient of friction. As the spacing between the dimples increases, there is a discernible decrease in the coefficient of friction values as evident for the samples with $\epsilon = 0.30$ and 0.12 . Additionally, for samples with the deeper dimples ($\epsilon = 0.30$), there is a more pronounced variation in the coefficient of friction across the different texture densities, i.e. the range between sample A and sample D is 0.08. In contrast, the values remain relatively consistent across the different texture densities for samples with the shallower dimples ($\epsilon = 0.06$), i.e. the range between sample I and sample L is 0.01.

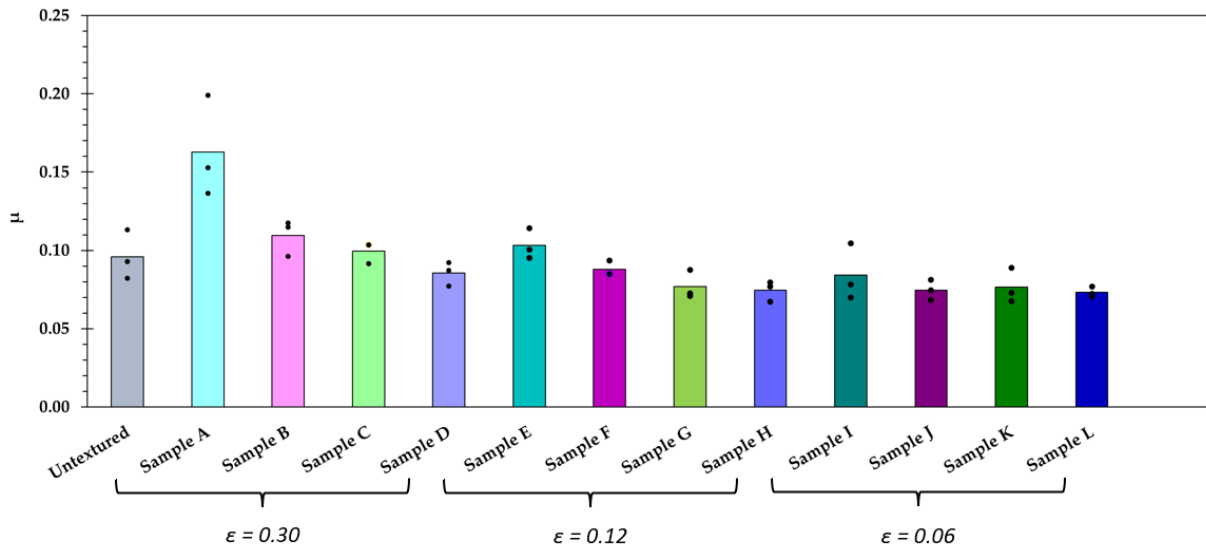


Fig. 7.1: Summary of results for friction data of the different textured samples

Table 7.1: Coefficient of friction values with percent differences of the different textured samples compared to the untextured sample

Sample	Avg. Friction	Std. Dev.	% Diff.
Untextured	0.096	0.016	-
Sample A	0.163	0.032	69.8
Sample B	0.110	0.012	14.2
Sample C	0.100	0.007	3.7
Sample D	0.086	0.008	-10.8
Sample E	0.103	0.010	7.6
Sample F	0.088	0.005	-8.4
Sample G	0.077	0.009	-19.8
Sample H	0.075	0.007	-22.3
Sample I	0.084	0.018	-12.2
Sample J	0.075	0.006	-22.1
Sample K	0.076	0.011	-20.3
Sample L	0.073	0.003	-23.6

Taking a closer look at the coefficient of friction vs. distance graphs shown in Fig. 7.2, sample A displays erratic and elevated friction behavior during the running-in phase as compared to sample D, which is stable throughout the duration of testing. This can be explained by the protuberances that form around the edges of the dimples during the laser-engraving process as can be seen in Fig. 5.3(a). The closer the dimples are to each other, the more interference is expected from the protuberances around the dimples, causing an increase in the interaction of asperities between the two surfaces, thus increasing the frictional force during sliding contact.

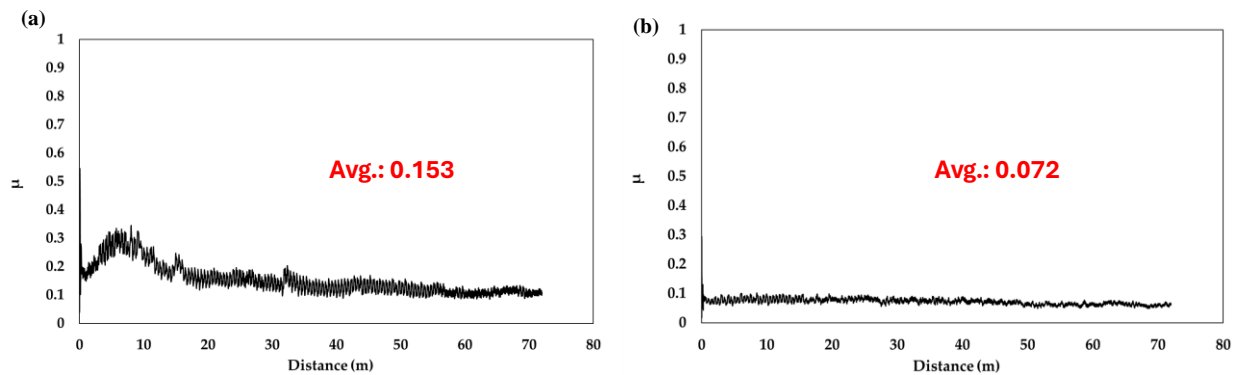


Fig. 7.2: Coefficient of friction values over distance of (a) sample A, and (b) sample L.

The most wear is observed in sample A in terms of wear depth and width, as can be seen in Fig. 7.3 and 7.4. This is likely due to third-body abrasive wear that results from wear particles generated when the protuberances around the dimples flatten during sliding contact. The main wear mechanism observed is adhesive wear caused by the plastic deformation of the softer surface, UHMWPE sliding against the harder ceramic surface. It is interesting to note that the width of the wear scar significantly decreases for sample I which is of the same texture density but of lower aspect ratio than samples A and E, which display high wear. This is indicative of a potential shift from the boundary lubrication regime to the mixed lubrication regime in the Stribeck curve in which a small hydrodynamic boost would separate the two surfaces and reduce the wear width. Samples I-L have similar wear patterns to each other and are observed to be more superficial than the wear found on the untextured sample, indicating improved wear behavior on the samples with $\varepsilon = 0.06$. Fig. 7.4 shows the profilometry scans for samples A and L. The wear depth of sample A is almost double that of sample L.

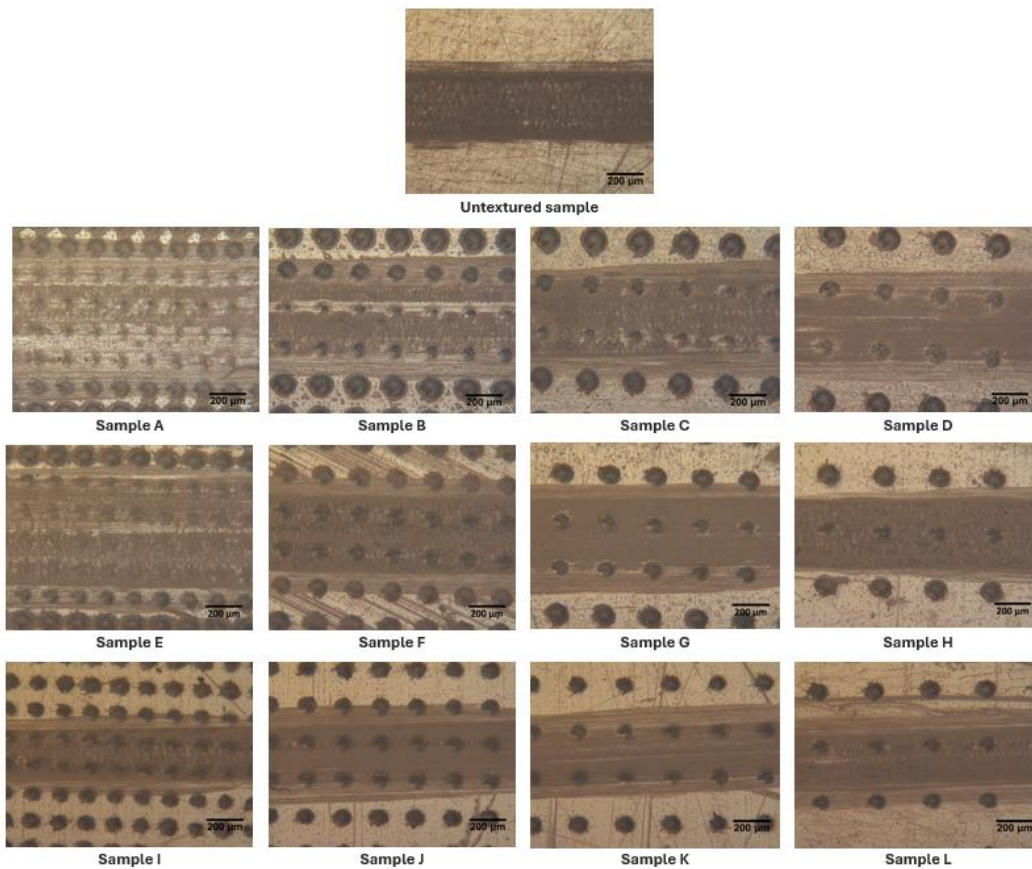


Fig. 7.3: Wear scars for textured samples

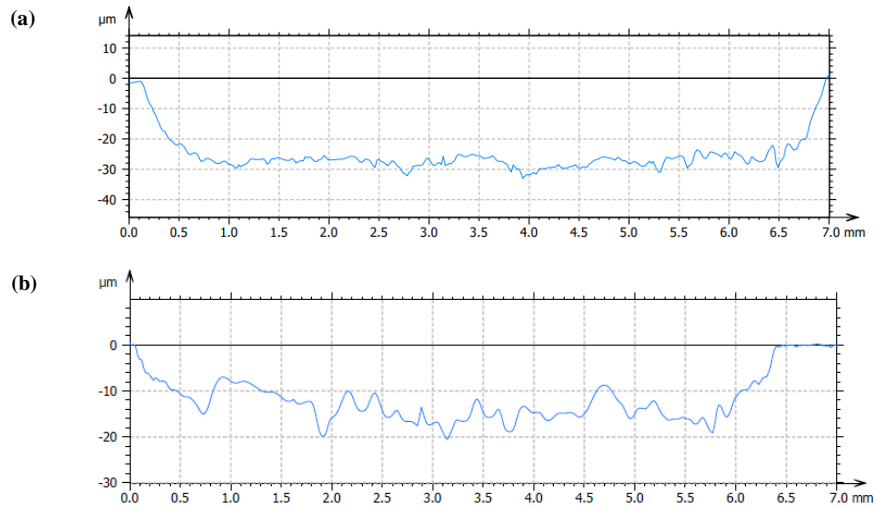


Fig. 7.4: Longitudinal cross-section of wear tracks for (a) sample A of dimple depth 30 μm , and (b) sample L of dimple depth 6 μm from profilometry

A two-way ANOVA analysis was done to reveal the significance of the dimple aspect ratio and texture density on the coefficient of friction. Specifically, the dimple aspect ratio significantly influenced the coefficient of friction, with dimples of $\varepsilon = 0.30$ resulting in the highest mean friction coefficient and dimples of $\varepsilon = 0.06$ in the lowest, $F(2, 24) = 26.78$, $p < 0.05$. Similarly, texture density showed a significant impact, where higher texture densities generally led to higher mean coefficients of friction compared to lower texture densities, $F(3, 24) = 15.43$, $p < 0.05$. Additionally, there was a significant interaction effect between the dimple aspect ratio and the texture density, $F(6, 24) = 4.05$, $p < 0.05$, indicating that the influence of the dimple aspect ratio on friction depends on the texture density level. For instance, at the highest aspect ratio, the coefficient of friction for the highest texture density was substantially higher than at low texture densities. These findings underscore the necessity of considering both dimple aspect ratio and texture density in unison when optimizing surface designs for frictional performance.

There are some limitations to this experiment. The ball-on-flat apparatus does not closely simulate the hip joints which exhibit conformal contact. The apparatus exhibits an overly-simplified subset of non-conformal contact in which the load distribution is concentrated at a much smaller contact area than in conformal contact. Because of this, the contact pressure is much higher than what is normal in the human hip joint. Furthermore, the apparatus only considers unidirectional motion as compared to the human hip joint which displays complex, multi-directional motion, which would

require a more complex apparatus to simulate accurately. However, the current apparatus is sufficient since the main goals of this research were to examine the effects of dimple aspect ratio and texture density and to compare them in terms of tribological performance.

7.2. Analytical Results

A numerical model was developed to compare the bearing load-carrying capacity for the different textured samples. Since the experimental apparatus has limitations when it comes to defining the desired lubrication regime, this numerical model can help us evaluate the approximate performance of the textures if sliding contact was to enter the hydrodynamic lubrication regime. The same operating conditions (δ and λ) used by Chyr et al. [44] were adopted in this model since the end goal was to compare the bearing load-carrying capacity rather than to get accurate film pressure values. Fig. 7.5 shows the typical non-dimensional film pressure distribution over a column of three dimples.

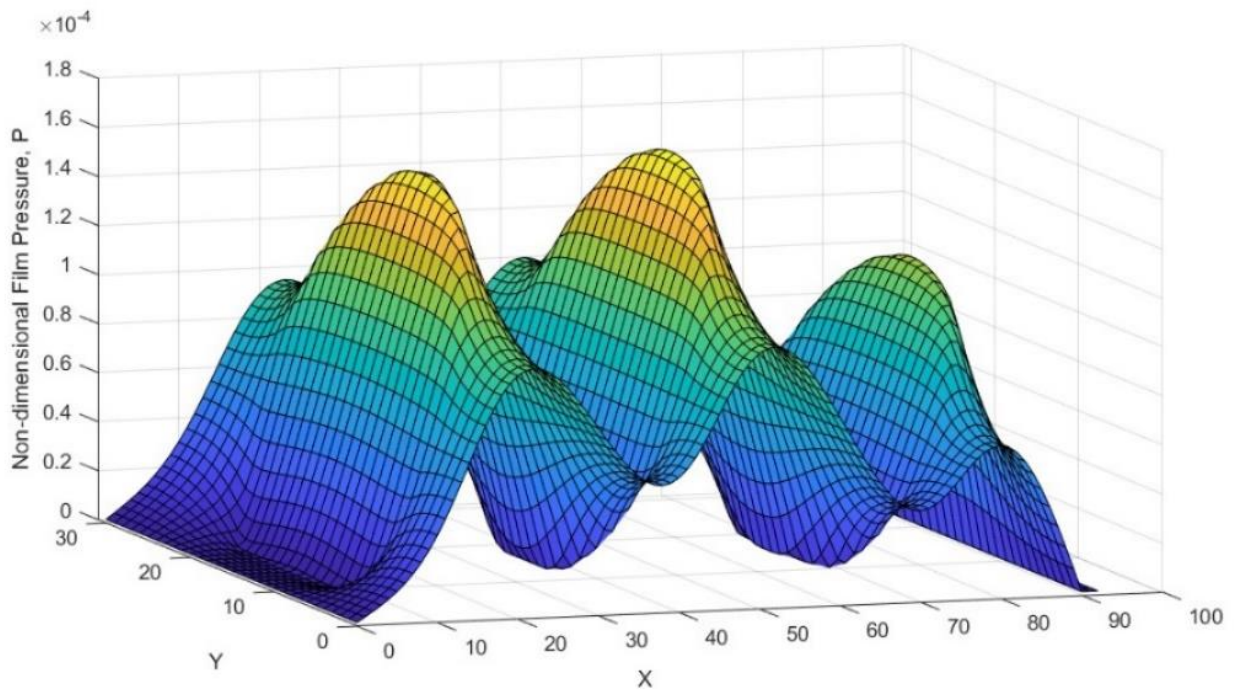


Fig. 7.5: Hydrodynamic pressure over a column of three dimples

The hydrodynamic lubrication model implemented in this study points to a greater hydrodynamic boost in dimples with the highest aspect ratio, $\epsilon = 0.30$. According to Fig. 7.6, samples C and D would lead to the largest hydrodynamic boost, and therefore, can be expected to perform best tribologically in the hydrodynamic lubrication regime. This behavior is opposite to what was seen experimentally in the boundary and/or mixed lubrication regime. Literature records instances where dimples with high aspect ratios store lubricant away from contact surfaces which negatively impacts lubrication [46], although mathematically, they are shown to create the largest hydrodynamic boost. However, one trend observed in both regimes is that the samples with $\epsilon = 0.30$ display the highest variation in performance, both in terms of the coefficient of friction experimentally, as well as the hydrodynamic boost in the numerical model.

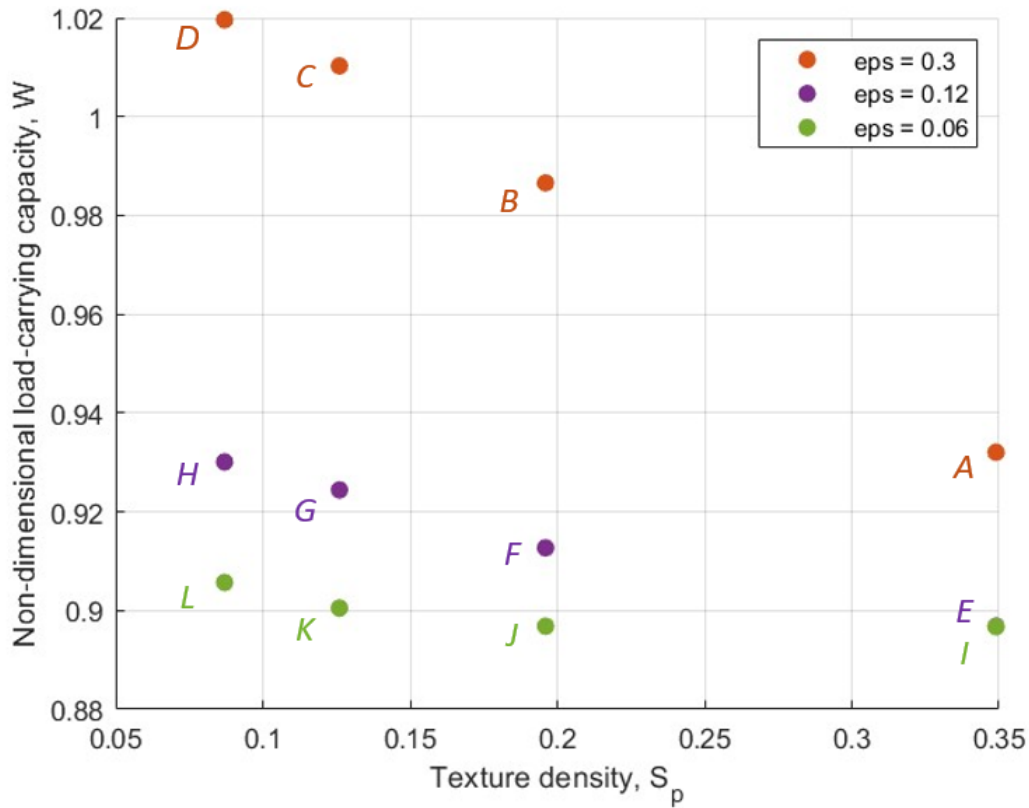


Fig. 7.6: Non-dimensional load-carrying capacity as a function of dimple aspect ratio and texture density

Since manufacturing tolerances were not held accurately during laser texturing, the corresponding calculations for the aspect ratio and texture density were done using nominal values for the dimple diameter and depth. Furthermore, experiments were done in the boundary or mixed lubrication regime so wear could be observed for characterization and due to the limitations of the apparatus, while the numerical model was for the hydrodynamic lubrication regime. For these reasons, the experimental and numerical results could not be compared. However, the model was an extension to the experiment and used to approximate the textured samples' tribological performance in the hydrodynamic lubrication regime.

8. CONCLUSION

In this study, ball-on-flat tribometer testing was carried out on CoP contacts and shown that polyethylene wear and the friction between the bearing surfaces could be reduced by adding circular dimples of a specific aspect ratio and texture density to the polyethylene surface. The conclusions can be summarized as follows:

- i. Samples with lower texture densities generally performed best in terms of friction and wear in the experiments likely due to less accumulation of material around the dimple edges during laser engraving process. There was a clear decreasing trend in both the coefficient of friction and wear depth/width with decreasing texture densities with the same aspect ratio group
- ii. Sample L ($\varepsilon = 0.06, S_p = 0.087$), the sample with the lowest texture density and dimple aspect ratio, yielded the lowest coefficient of friction and wear compared to the other textures. Sample L exhibited a 24% reduction in friction, while sample A exhibited a 70% increase in friction compared to the untextured sample
- iii. Experimentally, samples with lower texture densities and aspect ratios generally performed better in terms of friction and wear in the boundary/mixed lubrication regime. Numerically, samples with higher texture densities and aspect ratios led to the largest hydrodynamic boost which in turn, would lead to lower friction and wear in the hydrodynamic lubrication regime. However, in both cases, the range of variation is highest in the samples with $\varepsilon = 0.30$ across the different texture densities, while the samples with $\varepsilon = 0.06$ perform similar to each other

The results from this study clearly point to the texture density and dimple aspect ratio to having significant impact on the tribological behavior of the bearing surfaces. Additional studies where the hip joint conditions are mimicked more closely will need to be done to determine the ideal texture geometries for different material combinations. This can help optimize texture designs with the eventual goal of personalizing the textures to suit the end user in terms of factors such as their age, activity level, and weight.

9. SCOPE FOR FUTURE WORK

- i. Experimentally determine the appropriate testing parameters (load, frequency, stroke length, time) to emulate the different lubrication regimes on the ball-on-flat tribometer for untextured ceramic-on-polyethylene contact with artificial synovial fluid
- ii. Experimentally test the different textures in the hydrodynamic lubrication regime
- iii. Investigate the calculation of the lambda ratio, λ used to determine the lubrication regime for textured surfaces
- iv. Implement the elasto-hydrodynamic lubrication model for hard-on-soft contacts for select textures to account for the effects on the lubricant pressure due to the softer surface deforming much more than the harder surface

10. SOCIETAL CONTEXT

Several literatures have projected an increasing demand in THA in the coming years. A 2017 study [47] based on 20 countries part of the Organization of Economic Cooperation and Development (OECD), reported a projected increase in the demand for hip implants from 184 per 100,000 total population in the year 2015 to 275 in the year 2050 with the US contributing to 46% of hip implants in 2015 to a projected 56% in 2050. Although the procedure has been shown to have a high success rate, what was once reserved for an older, low-activity level population is now becoming a prevalent procedure within younger and more active cohorts. The finite lifespan of these implants calls for the rTHA, which creates a financial burden for the patients and the healthcare system and poses several surgical risks as compared to the pTHA [3]. Thus, research in the area of surface modification such as surface texturing is valuable in determining its ability to reduce friction and wear in artificial hip joint surfaces. Furthermore, with the rise in popularity and success of personalized medicine, this research will also enable the development of artificial hip implants to perform optimally for each, individual by factoring in inputs such as anatomy, body mass, and lifestyle activity level [24].

Surface texturing as a means of surface modification is being explored in other fields as well. For example, several studies have displayed the positive tribological performance of internal combustion engines (ICE) through the introduction of surface textures on either the piston rings or the cylinder liners. Koszela et al. [48] reported improved functional properties of the ICE with cylinder surface texturing. An increase in the maximum power of 5.1% was observed for ICEs with textured cylinders and a 5.8% increase for those with textured cylinders and DLC coating. Another application of surface texturing can be seen in journal bearings. Galda et al. [49] experimentally demonstrated that surface textures significantly affected the friction coefficient and found that textured journal bearings remain in hydrodynamic lubrication for longer and moved to mixed lubrication at lower speeds compared to smooth journal bearings.

The proposed research will help gain insight into the tribological behavior of surface-textured CoP hip implant surfaces and add to the characterization of wear mechanisms.

APPENDICES

Appendix A: Calculation of Lambda ratio, λ

For elliptical contact, the following equations developed by Hamrock and Dowson [50] are most widely used to calculate the minimum film thickness.

$$\lambda = \frac{h_{min}}{\sqrt{R_1^2 + R_2^2}}$$

$$\frac{h_{min}}{R'} = 3.63U^{0.68}G^{0.49}W^{-0.073}(1 - e^{-0.68k})$$

$$U = \frac{\eta_0 u_0}{E'R'}$$

$$G = \alpha E'$$

$$W = \frac{F}{E'R'^2}$$

where η_0 is the dynamic viscosity of the lubricant at atmosphere pressure under a certain temperature, u_0 is the mean speed of the two surfaces, R' is the effective radius, α is the pressure-viscosity coefficient under a certain temperature, F is the normal load, and k is the ellipticity parameter. According to ISO/TR 1281-2, 2008, the pressure viscosity coefficient α can be calculated from the kinematic viscosity, ν_0 .

Ceramic (Al₂O₃)						
E ₁	[Pa]	2.80E+11				
v ₁	[-]	0.23				
R ₁	[μ m]	0.105			E'	[MPa] 1.70E+03
UHMWPE						
E ₂	[Pa]	6.80E+08				
v ₂	[-]	0.45				
R ₂	[μ m]	0.064				

Lubricant	Dynamic Viscosity, η_0 at 24°C (N-s/mm ²)	Density, ρ (g/mm ³)	Kinematic Viscosity, ν_0 (mm ² /s)	Mean Speed, u_0 (mm/s)	Pressure-Viscosity Coefficient, α	Normal Load, F (N)	Effective Radius, R (mm)	Roughness (μm)
ASF	4.97E-08	0.001	4.44E-05	20	4.88E-03	5	3	0.122967475

Lubrication Regime for ceramic-PE contacts at 24°C dynamic Viscosity							
Lubricant	Dimensionless Speed Parameter, U	Dimensionless Material Parameter, G	Dimensionless Load Parameter, W	Ellipticity Parameter, k	h_{min}	λ	Lubrication Regime
s	1.95E-10	8.30E+00	3.27E-04	1	6.79E-06	5.52E-05	Boundary

$\lambda < 1$	Boundary lubrication regime
$1 < \lambda < 3$	Mixed lubrication regime
$\lambda > 3$	Full film lubrication regime

Appendix B: Staggered-Grid Finite Difference Equations to solve the Hydrodynamic Lubrication Model

2-D steady-state incompressible Reynolds' Equation:

$$\frac{\partial}{\partial x} \left(h^3 \frac{\partial p}{\partial x} \right) + \frac{\partial}{\partial y} \left(h^3 \frac{\partial p}{\partial y} \right) = 6\eta U \frac{dh}{dx}$$

After non-dimensionalization:

$$\frac{\partial}{\partial X} \left(H^3 \frac{\partial P}{\partial X} \right) + \frac{\partial}{\partial Y} \left(H^3 \frac{\partial P}{\partial Y} \right) = \frac{\lambda}{\delta^2} \frac{dH}{dX}$$

Applying finite difference equations:

$$\begin{aligned} \frac{\partial}{\partial X} \left(H^3 \frac{\partial P}{\partial X} \right) &= \frac{H_{i,j+0.5}^3 P_{i,j+1} + H_{i,j-0.5}^3 P_{i,j-1} - (H_{i,j+0.5}^3 + H_{i,j-0.5}^3) P_{i,j}}{\Delta x^2} \\ \frac{\partial}{\partial Y} \left(H^3 \frac{\partial P}{\partial Y} \right) &= \frac{H_{i+0.5,j}^3 P_{i+1,j} + H_{i-0.5,j}^3 P_{i-1,j} - (H_{i+0.5,j}^3 + H_{i-0.5,j}^3) P_{i,j}}{\Delta y^2} \\ \frac{\lambda}{\delta^2} \frac{dH}{dX} &= \frac{\lambda}{\delta^2} \frac{(H_{i,j+1} - H_{i,j-1})}{2\Delta x} \end{aligned}$$

Simplifying algebraically:

$$\begin{aligned} H_{i,j+0.5}^3 P_{i,j+1} + H_{i,j-0.5}^3 P_{i,j-1} + \left(\frac{\Delta x}{\Delta y} \right)^2 (H_{i+0.5,j}^3 P_{i+1,j} + H_{i-0.5,j}^3 P_{i-1,j}) - \frac{\lambda}{\delta^2} \frac{(H_{i,j+1} - H_{i,j-1})}{2} \Delta x \\ = (H_{i,j+0.5}^3 + H_{i,j-0.5}^3) P_{i,j} + \left(\frac{\Delta x}{\Delta y} \right)^2 (H_{i+0.5,j}^3 + H_{i-0.5,j}^3) P_{i,j} \end{aligned}$$

Since $\frac{\Delta x}{\Delta y} = 1$:

$$\begin{aligned} H_{i,j+0.5}^3 P_{i,j+1} + H_{i,j-0.5}^3 P_{i,j-1} + H_{i+0.5,j}^3 P_{i+1,j} + H_{i-0.5,j}^3 P_{i-1,j} - \frac{\lambda}{\delta^2} \frac{(H_{i,j+1} - H_{i,j-1})}{2} \Delta x \\ = (H_{i,j+0.5}^3 + H_{i,j-0.5}^3 + H_{i+0.5,j}^3 + H_{i-0.5,j}^3) P_{i,j} \end{aligned}$$

$$P_{i,j} = A_{i,j} P_{i,j+1} + B_{i,j} P_{i,j-1} + C_{i,j} P_{i+1,j} + D_{i,j} P_{i-1,j} + E_{i,j}$$

$$\text{denom.} = (H_{i,j+0.5}^3 + H_{i,j-0.5}^3 + H_{i+0.5,j}^3 + H_{i-0.5,j}^3)$$

$$A_{i,j} = \frac{H_{i,j+0.5}^3}{denom.}$$

$$B_{i,j} = \frac{H_{i,j-0.5}^3}{denom.}$$

$$C_{i,j} = \frac{H_{i+0.5,j}^3}{denom.}$$

$$D_{i,j} = \frac{H_{i-0.5,j}^3}{denom.}$$

$$E_{i,j} = \frac{\lambda}{\delta^2} \frac{(H_{i,j+1} - H_{i,j-1})}{2 \cdot denom} \Delta x$$

Appendix C: Two-way ANOVA Analysis for Coefficient of Friction Data

	Sp = .35	Sp = .2	Sp = .13	Sp = .09
eps = 0.3	0.199	0.115	0.103	0.092
	0.137	0.118	0.103	0.087
	0.153	0.096	0.092	0.077
eps = 0.12	0.114	0.094	0.072	0.077
	0.095	0.085	0.071	0.080
	0.100	0.085	0.087	0.067
eps = 0.06	0.070	0.068	0.068	0.072
	0.078	0.081	0.089	0.077
	0.105	0.075	0.073	0.071

Null hypotheses:

- H1 No difference in means of the different aspect ratio groups
- H2 No difference in means of the different texture density groups
- H3 No interaction between the aspect ratio and texture density

Anova: Two-Factor With Replication

SUMMARY Sp = .35 Sp = .2 Sp = .13 Sp = .09 Total

eps = 0.3

	3	3	3	3	12
Count	3	3	3	3	12
Sum	0.488603	0.328553	0.298539	0.25679	1.372486
Average	0.162868	0.109518	0.099513	0.085597	0.114374
Variance	0.001054	0.000138	4.6E-05	5.88E-05	0.00117

eps = 0.12

	3	3	3	3	12
Count	3	3	3	3	12
Sum	0.309736	0.263557	0.230665	0.223536	1.027494
Average	0.103245	0.087852	0.076888	0.074512	0.085624
Variance	9.67E-05	2.48E-05	8.42E-05	4.25E-05	0.000186

eps = 0.06

	3	3	3	3	12
Count	3	3	3	3	12
Sum	0.252691	0.22415	0.229299	0.219817	0.925957
Average	0.08423	0.074717	0.076433	0.073272	0.077163
Variance	0.000327	4.22E-05	0.000122	9.92E-06	0.000111

Total

	9	9	9	9
Count	9	9	9	9
Sum	1.05103	0.81626	0.758503	0.700143
Average	0.116781	0.090696	0.084278	0.077794
Variance	0.001632	0.000283	0.000194	6.23E-05

ANOVA

Source of Varia	SS	df	MS	F	P-value	F crit
Sample	0.009131	2	0.004566	26.78447	7.70E-07	3.402826
Columns	0.00789	3	0.00263	15.42916	8.37E-06	3.008787
Interactor	0.004143	6	0.000691	4.051244	0.006057	2.508189
Within	0.004091	24	0.00017			

Appendix D: MATLAB Code

```
%% Pattered Microtexture Design
% Sandhya Vaidyanathan
% MS Thesis
% 2023-24

clear; clc; close all;

%% Bearing operating conditions:
mu = 4.97E-08; % N/mm2.s
U = 20; % mm/s
rp = 1;
p0 = 1; % N/mm2
p_cav = .9;
c = 5.53E-08*1000; % mm
% Non-dimensional flow factor:
lambda = 5.94*10(-4); % 3*mu*U/2/rp/p0;
% Non-dimensional minimum spacing:
delta = 0.01; % c/2/rp;
N = 7;

%% Aspect ratio .3:
eps = .3;

% Texture A:
% Texture density:
Sp = .349;
[W] = ReynoldsCalc(eps,Sp,N,lambda,delta,p_cav,p0);
figure
scatter(Sp,W,[],"MarkerFaceColor","#D95319","MarkerEdgeColor","#D95319")
hold on

% Texture B:
% Texture density:
Sp = .196;
[W] = ReynoldsCalc(eps,Sp,N,lambda,delta,p_cav,p0);
scatter(Sp,W,[],"MarkerFaceColor","#D95319","MarkerEdgeColor","#D95319")
hold on

% Texture C:
% Texture density:
Sp = .126;
[W] = ReynoldsCalc(eps,Sp,N,lambda,delta,p_cav,p0);
scatter(Sp,W,[],"MarkerFaceColor","#D95319","MarkerEdgeColor","#D95319")
hold on

% Texture D:
% Texture density:
Sp = .087;
[W] = ReynoldsCalc(eps,Sp,N,lambda,delta,p_cav,p0);
scatter(Sp,W,[],"MarkerFaceColor","#D95319","MarkerEdgeColor","#D95319")
hold on
```

```

%% Aspect ratio .12:
eps = .12;

% Texture E:
% Texture density:
Sp = .349;
[W] = ReynoldsCalc(eps,Sp,N,lambda,delta,p_cav,p0);
scatter(Sp,W,[],"MarkerFaceColor","#7E2F8E","MarkerEdgeColor","#7E2F8E")
hold on

% Texture F:
% Texture density:
Sp = .196;
[W] = ReynoldsCalc(eps,Sp,N,lambda,delta,p_cav,p0);
scatter(Sp,W,[],"MarkerFaceColor","#7E2F8E","MarkerEdgeColor","#7E2F8E")
hold on

% Texture G:
% Texture density:
Sp = .126;
[W] = ReynoldsCalc(eps,Sp,N,lambda,delta,p_cav,p0);
scatter(Sp,W,[],"MarkerFaceColor","#7E2F8E","MarkerEdgeColor","#7E2F8E")
hold on

% Texture H:
% Texture density:
Sp = .087;
[W] = ReynoldsCalc(eps,Sp,N,lambda,delta,p_cav,p0);
scatter(Sp,W,[],"MarkerFaceColor","#7E2F8E","MarkerEdgeColor","#7E2F8E")

%% Aspect ratio .06:
eps = .06;

% Texture I:
% Texture density:
Sp = .349;
[W] = ReynoldsCalc(eps,Sp,N,lambda,delta,p_cav,p0);
scatter(Sp,W,[],"MarkerFaceColor","#77AC30","MarkerEdgeColor","#77AC30")
hold on

% Texture J:
% Texture density:
Sp = .196;
[W] = ReynoldsCalc(eps,Sp,N,lambda,delta,p_cav,p0);
scatter(Sp,W,[],"MarkerFaceColor","#77AC30","MarkerEdgeColor","#77AC30")
hold on

% Texture K:
% Texture density:
Sp = .126;
[W] = ReynoldsCalc(eps,Sp,N,lambda,delta,p_cav,p0);
scatter(Sp,W,[],"MarkerFaceColor","#77AC30","MarkerEdgeColor","#77AC30")

```

```

hold on

% Texture L:
% Texture density:
Sp = .087;
[W] = ReynoldsCalc(eps,Sp,N,lambda,delta,p_cav,p0);
scatter(Sp,W,[],"MarkerFaceColor","#77AC30","MarkerEdgeColor","#77AC30")

hold off
grid on
xlabel('Texture density, S_p')
ylabel('Non-dimensional load-carrying capacity, W')
legend('eps = 0.3',' ',' ','eps = 0.12',' ',' ','eps = 0.06',' ',' ','')

% Function to calculate load-bearing capacity of per unit area:
function [W] = ReynoldsCalc(eps,Sp,N,lambda,delta,p_cav,p0)
% Mesh grid set-up:
% Number of nodes (ODD #):
m = 301;
n = m;
m_ = 2*m-1;
n_ = 2*n-1;
% Initializing X and Y arrays:
X = NaN(m_,N*n_);
Y = NaN(m_,N*n_);
% Side length per cell (based on texture density):
Lx = 2*sqrt(pi/4/Sp);
Ly = Lx;
% Distance between nodes:
dx = Lx/(m-1);
dy = Ly/(n-1);

% Populating X array:
for Cm = 1:N % Cm is the index for dimple count
    X(:,1+(Cm-1)*m_) = -Lx/2; % Populating first column of each unit cell - X
array
    for i = 2+(Cm-1)*m_:m_+(Cm-1)*m_ % Populating rest of unit cell - X array
        X(:,i) = X(:,i-1)+dx/2;
    end
end

% Populating Y array:
Y(1,:) = Ly/2; % Populating first row of all the unit cells - Y array
for j = 2:n_
    Y(j,:) = Y(j-1,:)-dy/2; % Populating rest of unit cell - Y array
end

% Calculate non-dimensional local clearance:
% Dimple top view:
top_view = sqrt(X.^2+Y.^2); % to determine if we are inside or outside dimple later
% figure
% surf(top_view)

```



```

% H(X,Y):
H = NaN(m_,N*n_);
for i = 1:m_
    for j = 1:N*n_
        if top_view(i,j) > 1 % outside dimple
            H(i,j)= 1;
        else % inside/on dimple
            % H(i,j) = 1 + E/delta; % cylindrical dimples
            H(i,j) = 1+1/(2*delta)*sqrt((eps+1/(4*eps))^2 ...
                -(top_view(i,j))^2)-1/(2*delta)*(1/(4*eps)-eps); % spherical dimples
        end
    end
end
% figure
% surf(H)

% Pressure calculation:
P = zeros(m,N*n);
p_in = 1;
p_out = 1;
P(:,1) = p_in;
P(:,n*N) = p_out;
w = 1.4; % over-relaxation factor
e_crit = 10^(-2);
max_iter = 5000;
for k = 1:max_iter
    P_old = P;
    for i = 2:m-1
        for j = 2:N*(n-1)
            denom = H(2*i+1,2*j)^3 + H(2*i-1,2*j)^3 + H(2*i,2*j+1)^3 + H(2*i,2*j-
1)^3;
            A = H(2*i,2*j+1)^3/denom;
            B = H(2*i,2*j-1)^3/denom;
            C = H(2*i+1,2*j)^3/denom;
            D = H(2*i-1,2*j)^3/denom;
            E = (-lambda/delta^2*dx/2*(H(i,j+1) - H(i,j-1)))/denom;
            P(i,j) = (1-w)*P(i,j)+w*(A*P(i,j+1)+B*P(i,j-1)+C*P(i+1,j)+D*P(i-1,j)+E);
            if P(i,j) < p_cav
                P(i,j) = p_cav;
            end
        end
    end
    P(:,1) = p_in; % Inlet boundary condition
    P(:,N*n) = p_out; % Outlet boundary condition
    P(1,:) = P(2,:); % Top boundary (dp/dy = 0)
    P(m,:) = P(m-1,:); % Bottom boundary (dp/dy = 0)
    err = max(abs((P-P_old)./P_old),[], 'all');
    if err < e_crit
        break;
    end
end
if k < max_iter

```

```
        fprintf('Convergence has been reached\n')
else
    fprintf('Convergence not reached\n')
end
W = sum(P, 'all')/(Lx*Ly*N);

% figure
% surf(P)
% xlabel('X')
% ylabel('Y')
% zlabel('Pressure')
end
```

REFERENCES

- [1] Borjali, A., Langhorn, J., Monson, K., and Raeymaekers, B., 2017, “Using a Patterned Microtexture to Reduce Polyethylene Wear in Metal-on-Polyethylene Prosthetic Bearing Couples,” *Wear*, **392–393**, pp. 77–83.
- [2] Foran, J. R. H., “Total Hip Replacement,” OrthoInfo - AAOS.
- [3] Schwartz, A. M., Farley, K. X., Guild, G. N., and Bradbury, T. L., 2020, “Projections and Epidemiology of Revision Hip and Knee Arthroplasty in the United States to 2030,” *J. Arthroplasty*, **35**(6), pp. S79–S85.
- [4] Abu-Amer, Y., Darwech, I., and Clohisy, J. C., 2007, “Aseptic Loosening of Total Joint Replacements: Mechanisms Underlying Osteolysis and Potential Therapies,” *Arthritis Res. Ther.*, **9**(Suppl 1), p. S6.
- [5] Ghosh, S., and Abanteriba, S., 2016, “Status of Surface Modification Techniques for Artificial Hip Implants,” *Sci. Technol. Adv. Mater.*, **17**(1), pp. 715–735.
- [6] Nečas, D., Usami, H., Niimi, T., Sawae, Y., Křupka, I., and Hartl, M., 2020, “Running-in Friction of Hip Joint Replacements Can Be Significantly Reduced: The Effect of Surface-Textured Acetabular Cup,” *Friction*, **8**(6), pp. 1137–1152.
- [7] Di Puccio, F., and Mattei, L., 2015, “Biotribology of Artificial Hip Joints,” *World J. Orthop.*, **6**(1), pp. 77–94.
- [8] Williams, J. A., 2005, *Engineering Tribology*, Cambridge University Press, New York.
- [9] Wang, Q. J., and Chung, Y.-W., eds., 2013, *Encyclopedia of Tribology*, Springer US, Boston, MA.
- [10] Nogués, C., Blanquer, A., Barrios, L., and Ibañez, E., 2018, “Assessment of Metallic Alloys Biocompatibility,” *Biomaterials in Clinical Practice*, F. Zivic, S. Affatato, M.

Trajanovic, M. Schnabelrauch, N. Grujovic, and K.L. Choy, eds., Springer International Publishing, Cham, pp. 461–475.

- [11] Merola, M., and Affatato, S., 2019, “Materials for Hip Prostheses: A Review of Wear and Loading Considerations,” *Materials*, **12**(3).
- [12] Shekhawat, D., Singh, A., Bhardwaj, A., and Patnaik, A., 2021, “A Short Review on Polymer, Metal and Ceramic Based Implant Materials,” *IOP Conf. Ser. Mater. Sci. Eng.*, **1017**(1), p. 012038.
- [13] Drummond, J., Tran, P., and Fary, C., 2015, “Metal-on-Metal Hip Arthroplasty: A Review of Adverse Reactions and Patient Management,” *J. Funct. Biomater.*, **6**(3), pp. 486–499.
- [14] Hu, C. Y., and Yoon, T.-R., 2018, “Recent Updates for Biomaterials Used in Total Hip Arthroplasty,” *Biomater. Res.*, **22**(1), p. 33.
- [15] Affatato, S., Jaber, S. A., and Taddei, P., 2018, “Ceramics for Hip Joint Replacement,” *Biomaterials in Clinical Practice*, F. Zivic, S. Affatato, M. Trajanovic, M. Schnabelrauch, N. Grujovic, and K.L. Choy, eds., Springer International Publishing, Cham, pp. 167–181.
- [16] Davim, J. P., 2010, *Biotribology*, ISTE ; John Wiley & Sons, London : Hoboken, NJ.
- [17] Heckmann, N. D., Sivasundaram, L., Stefl, M. D., Kang, H. P., Basler, E. T., and Lieberman, J. R., 2018, “Total Hip Arthroplasty Bearing Surface Trends in the United States From 2007 to 2014: The Rise of Ceramic on Polyethylene,” *J. Arthroplasty*, **33**(6), pp. 1757-1763.e1.
- [18] Liu, Y., Rath, B., Tingart, M., and Eschweiler, J., 2020, “Role of Implants Surface Modification in Osseointegration: A Systematic Review,” *J. Biomed. Mater. Res. A*, **108**(3), pp. 470–484.

- [19] Jones, S. E., Nichols, L., Elder, S. H., and Priddy, L. B., 2023, "Laser Microgrooving and Resorbable Blast Texturing for Enhanced Surface Function of Titanium Alloy for Dental Implant Applications," *Biomed. Eng. Adv.*, **5**, p. 100090.
- [20] Shi, G., Yu, X., Meng, H., Zhao, F., Wang, J., Jiao, J., and Jiang, H., 2023, "Effect of Surface Modification on Friction Characteristics of Sliding Bearings: A Review," *Tribol. Int.*, **177**, p. 107937.
- [21] Shivakoti, I., Kibria, G., Cep, R., Pradhan, B. B., and Sharma, A., 2021, "Laser Surface Texturing for Biomedical Applications: A Review," *Coatings*, **11**(2), p. 124.
- [22] Riveiro, A., Maçon, A. L. B., Del Val, J., Comesaña, R., and Pou, J., 2018, "Laser Surface Texturing of Polymers for Biomedical Applications," *Front. Phys.*, **6**, p. 16.
- [23] Obilor, A. F., Pacella, M., Wilson, A., and Silberschmidt, V. V., 2022, "Micro-Texturing of Polymer Surfaces Using Lasers: A Review," *Int. J. Adv. Manuf. Technol.*, **120**(1–2), pp. 103–135.
- [24] Allen, Q., and Raeymaekers, B., 2021, "Surface Texturing of Prosthetic Hip Implant Bearing Surfaces: A Review," *J. Tribol.*, **143**(4).
- [25] Lu, P., and Wood, R. J. K., 2020, "Tribological Performance of Surface Texturing in Mechanical Applications-a Review," *Surf. Topogr. Metrol. Prop.*, **8**(4).
- [26] Affatato, S., Spinelli, M., Zavalloni, M., Mazzega-Fabbro, C., and Viceconti, M., 2008, "Tribology and Total Hip Joint Replacement: Current Concepts in Mechanical Simulation," *Med. Eng. Phys.*, **30**(10), pp. 1305–1317.
- [27] Dong, Y., Svoboda, P., Vrbka, M., Kostal, D., Urban, F., Cizek, J., Roupčova, P., Dong, H., Krupka, I., and Hartl, M., 2016, "Towards Near-Permanent CoCrMo Prosthesis Surface by Combining Micro-Texturing and Low Temperature Plasma Carburising," *J. Mech. Behav. Biomed. Mater.*, **55**, pp. 215–227.

- [28] Young, S. K., Lotito, M. A., and Keller, T. S., 1998, “Friction Reduction in Total Joint Arthroplasty,” *Wear*, **222**(1), pp. 29–37.
- [29] Lee, H., Lee, S., Park, J.-K., and Yang, M., 2018, “Friction and Wear Characteristics of Surface-Modified Titanium Alloy for Metal-on-Metal Hip Joint Bearing,” *Int. J. Precis. Eng. Manuf.*, **19**(6), pp. 917–924.
- [30] Tarabolsi, M., Klassen, T., Mantwill, F., Gärtner, F., Siegel, F., and Schulz, A., 2013, “Patterned CoCrMo and Al₂O₃ Surfaces for Reduced Free Wear Debris in Artificial Joint Arthroplasty,” *J. Biomed. Mater. Res. A*, **101**(12), pp. 3447–3456.
- [31] Sufyan, M., Hussain, M., Ahmad, H., Abbas, N., Ashraf, J., and Zahra, N., 2019, “Bulge Micro-Textures Influence on Tribological Performance of Ultra-High-Molecular-Weight-Polyethylene (UHMWPE) under Phosphatidylcholine (Lipid) and Bovine Serum Albumin (BSA) Solutions,” *Biomed. Phys. Eng. Express*, **5**(3), p. 035021.
- [32] Pratap, T., and Patra, K., 2020, “Tribological Performances of Symmetrically Micro-Textured Ti-6Al-4V Alloy for Hip Joint,” *Int. J. Mech. Sci.*, **182**, p. 105736.
- [33] Dougherty, P. S. M., Srivastava, G., Onler, R., Ozdoganlar, O. B., and Higgs, C. F., 2015, “Lubrication Enhancement for UHMWPE Sliding Contacts through Surface Texturing,” *Tribol. Trans.*, **58**(1), pp. 79–86.
- [34] Kashyap, V., and Ramkumar, P., 2019, “Feasibility Study of Micro-Groove Cross Hatched Surface Texturing on Ti6Al4V for Improved Biotribological Performance in Metal-on-Polymer Hip Implant,” *Tribol. - Mater. Surf. Interfaces*, **13**(3), pp. 150–160.
- [35] Cho, M., and Choi, H.-J., 2014, “Optimization of Surface Texturing for Contact Between Steel and Ultrahigh Molecular Weight Polyethylene Under Boundary Lubrication,” *Tribol. Lett.*, **56**(3), pp. 409–422.
- [36] Roy, T., Choudhury, D., Ghosh, S., Bin Mamat, A., and Pinguan-Murphy, B., 2015, “Improved Friction and Wear Performance of Micro Dimpled Ceramic-on-Ceramic Interface for Hip Joint Arthroplasty,” *Ceram. Int.*, **41**(1), pp. 681–690.

- [37] Cuervo, P., López, D. A., Cano, J. P., Sánchez, J. C., Rudas, S., Estupiñán, H., Toro, A., and Abdel-Aal, H. A., 2016, “Development of Low Friction Snake-Inspired Deterministic Textured Surfaces,” *Surf. Topogr. Metrol. Prop.*, **4**(2), p. 024013.
- [38] Kustandi, T. S., Choo, J. H., Low, H. Y., and Sinha, S. K., 2010, “Texturing of UHMWPE Surface via NIL for Low Friction and Wear Properties,” *J. Phys. Appl. Phys.*, **43**(1), p. 015301.
- [39] Wei, X., Li, W., Liang, B., Li, B., Zhang, J., Zhang, L., and Wang, Z., 2016, “Surface Modification of Co–Cr–Mo Implant Alloy by Laser Interference Lithography,” *Tribol. Int.*, **97**, pp. 212–217.
- [40] Ito, H., Kaneda, K., Yuhta, T., Nishimura, I., Yasuda, K., and Matsuno, T., 2000, “Reduction of Polyethylene Wear by Concave Dimples on the Frictional Surface in Artificial Hip Joints,” *J. Arthroplasty*, **15**(3), pp. 332–338.
- [41] Choudhury, D., Roy, T., Krupka, I., Hartl, M., and Mootanah, R., 2015, “Tribological Investigation of Ultra-High Molecular Weight Polyethylene against Advanced Ceramic Surfaces in Total Hip Joint Replacement,” *Proc. Inst. Mech. Eng. Part J J. Eng. Tribol.*, **229**(4), pp. 410–419.
- [42] Dantas, P., Gonçalves, S. R., Grenho, A., Mascarenhas, V., Martins, J., Tavares Da Silva, M., Gonçalves, S. B., and Guimarães Consciência, J., 2023, “Hip Joint Contact Pressure and Force: A Scoping Review of in Vivo and Cadaver Studies,” *Bone Jt. Res.*, **12**(12), pp. 712–721.
- [43] Qiu, M., Delic, A., and Raeymaekers, B., 2012, “The Effect of Texture Shape on the Load-Carrying Capacity of Gas-Lubricated Parallel Slider Bearings,” *Tribol. Lett.*, **48**(3), pp. 315–327.
- [44] Chyr, A., Qiu, M., Speltz, J. W., Jacobsen, R. L., Sanders, A. P., and Raeymaekers, B., 2014, “A Patterned Microtexture to Reduce Friction and Increase Longevity of Prosthetic Hip Joints,” *Wear*, **315**(1–2), pp. 51–57.

- [45] 2007, *Numerical Computation of Internal and External Flows*, Elsevier.
- [46] Ryk, G., Kligerman, Y., and Etsion, I., 2002, “Experimental Investigation of Laser Surface Texturing for Reciprocating Automotive Components,” *Tribol. Trans.*, **45**(4), pp. 444–449.
- [47] Pabinger, C., Lothaller, H., Portner, N., and Geissler, A., 2018, “Projections of Hip Arthroplasty in OECD Countries up to 2050,” *HIP Int.*, **28**(5), pp. 498–506.
- [48] Koszela, W., Pawlus, P., Reizer, R., and Liskiewicz, T., 2018, “The Combined Effect of Surface Texturing and DLC Coating on the Functional Properties of Internal Combustion Engines,” *Tribol. Int.*, **127**, pp. 470–477.
- [49] Galda, L., Sep, J., Olszewski, A., and Zochowski, T., 2019, “Experimental Investigation into Surface Texture Effect on Journal Bearings Performance,” *Tribol. Int.*, **136**, pp. 372–384.
- [50] Hamrock, B. J., and Dowson, D., 1976, “Isothermal Elastohydrodynamic Lubrication of Point Contacts. III: Fully Flooded Results,” NASA, Boston.